

A model-based approach for clinical evaluation of left ventricular deformation

Espen W. Remme

Norwegian University of Science and Technology

April 2004

A model-based approach for clinical evaluation of left ventricular deformation
Espen W. Remme

NTNU Trondheim
Norges teknisk-naturvitenskapelige universitet
Doktor ingeniøravhandling 2004:48
Institutt for teknisk kybernetikk
ITK-rapport 2004:4-W

ISBN 82-471-6304-9 (printed)
ISBN 82-471-6303-7 (electronic)
ISSN 1503-8181

Abstract

Assessment of left ventricular (LV) deformation is essential for clinical evaluation of LV function and cardiac images are frequently used to evaluate the LV motion and function. By combining the images with mathematical models more information may be extracted from the images. The work presented in this thesis has focused on using the finite element (FE) method to describe the LV and its deformation and combining this method with images of the heart to extract more information about the deformation.

We developed a method that estimated the LV deformation by manually tracking distinct anatomical landmarks (fiducial markers) through the cardiac cycle in 3 dimensional (3D) images of the heart. The motion of the nodal parameters of an FE mesh shaped to the geometry of the LV was fitted to the motion of the fiducial markers and thus provided a means to describe the motion. The sparsity of the fiducial markers made the fitting problem under-constrained so a parameter distribution model (PDM) of likely motions were constructed from a historical database of cases where FE meshes had been fitted to the motion of magnetic resonance (MR) tagged data. The estimated deformation from the fiducial marker fitting was filtered through the PDM and the resulting deformation corresponded well when compared to the deformation obtained from MR tagging in 13 normal subjects.

A method that decomposed the LV deformation into different deformation modes such as longitudinal shortening, wall thickening, and twisting was developed. The nodes of a subject's LV FE mesh were displaced according to each deformation mode and the relative contribution of each mode to the total deformation measured by MR tagging was quantified by calculating a coefficient for each mode. A study that compared 13 young normal subjects with 13 older diabetes patients showed that the patients had a significantly lower degree of longitudinal shortening and wall thickening but a higher degree of longitudinal twist.

The LV deformation is influenced by cardiac disease via the material properties of the myocardium. We investigated the effects of the material parameter values on the LV deformation in a simulation study using an FE model of the LV. A description of the myocardial microstructure and a passive and active constitutive law was included in the model. The cardiac cycle was simulated from the beginning of diastasis through to the end of ejection by applying appropriate boundary conditions. The different deformation modes between end diastole and end systole were extracted and quantified for different sets of material parameters. We found that stiffer material properties particularly in the myocardial sheet direction impaired longitudinal shortening and wall thickening.

A sensitivity analysis was carried out to look at the various material parameters' influence on LV wall strains during passive inflation. The analysis showed a high degree of coupling of the parameters in the constitutive law, which indicated an over-parameterization of the law. A parameter estimation study revealed the same problem. Most of the parameters were set to constant values and only one parameter in each of the three microstructural directions were estimated during the passive inflation phase using synthetic strain data as measurements. This still gave good estimates of the stress-strain relationships in the fiber and sheet directions.

Preface

This thesis is submitted to the Norwegian University of Science and Technology (NTNU) for partial fulfillment of the requirements of the degree of “Doktor Ingeniør”.

The project work has been carried out at the Department of Circulation and Medical Imaging, NTNU and at the Bioengineering Institute, University of Auckland, New Zealand. My supervisors have been Professor Bjørn Angelsen and Professor Peter Hunter. Professor Rolf Henriksen has served as the link to the Faculty of Information Technology, Mathematics and Electrical Engineering. The work has been supported by the Norwegian Research council: grants #128267/320 and #139327/300 and through a grant of computing time (Program for supercomputing), and by a scholarship from the Bioengineering Institute, University of Auckland.

Acknowledgements

There are many people that need to be acknowledged for their contribution to this project work. First I would like to thank my supervisor Professor Bjørn Angelsen who initially introduced me to biomedical engineering. He has always been very supportive of my ideas and given me much freedom and financial backup to pursue my strategy to carry out the project work.

The entire project has been dependent on Professor Peter Hunter’s support and hospitality to let me come and work at the Bioengineering Institute which I believe is one of the world’s finest research environments in heart mechanics. Peter also served as my supervisor, came up with new ideas for the project and got me extended financial support. Thank you very much, Peter. I also want to thank all the colleagues and work mates at the Bioengineering Institute for their great hospitality and generous helpfulness. In particular I want to mention Carey Stevens who I must have driven mad with all sorts of questions when I was first learning the software program CMISS. Also Leo Cheng, Kevin Augenstein, and Martyn Nash suffered a heavy burden of too many of my questions. I would like to give sincere thanks to Dr. Alistair Young for giving me access to magnetic resonance measurement data, and for good and valuable collaboration.

Many thanks go to Professor Fridtjov Irgens who showed keen interest in my project and supervised me through my initial studies of continuum and heart mechanics. I wish to thank Stein Inge Rabben, who in many ways served as my mentor, for much good advice – which has always been worth listening to.

Professor Otto Smiseth, Rikshospitalet, was very helpful when my initial plans for obtaining patient ultrasound data failed. I owe him great thanks for inviting me to record experimental data at his lab. Thanks also to Helge Skulstad, Stig Urheim, and Erik Lyseggen who helped me with those measurements.

Finally, former and present work mates at the Department of Circulation and Medical Imaging: Professor Hans Torp, Vidar Sørhus, Sigve Hovda, Bjarne Bergheim, Wibeke Nordhøy, Tonni Johansen, Olga Maltseva, Svein-Erik Måsøy, and Rune Hansen – thanks for all your professional help and also very welcomed and nice distractions from work.

Espen W. Remme

Auckland, April 2004

Contents

1	Introduction	1
1.1	Motivation	1
1.2	Aims of the Study	3
1.3	Contributions	4
1.4	Summary of Papers	5
2	Introduction to the Finite Element Method	8
3	Conclusions and Further Research	14
3.1	Conclusions	14
3.2	Directions for Further Research	15
	References	18

Paper A - Ventricular mechanics in diastole: material parameter sensitivity
Journal of Biomechanics, 36: 737-748, May 2003
C, Stevens, E. Remme, I. LeGrice, P. Hunter

Paper B - Development of an in vivo method for determining material properties of passive myocardium
Journal of Biomechanics, 37: 669-678, May 2004
E. W. Remme, P. J. Hunter, O. Smiseth, C. Stevens, S. I. Rabben, H. Skulstad, B. Angelsen

Paper C - Parameter distribution models for estimation of left ventricular deformation using sparse fiducial markers
Submitted for publication
E. W. Remme, K. F. Augenstein, A. A. Young, P. J. Hunter

Paper D - Extraction and quantification of left ventricular deformation modes
IEEE Transactions on Biomedical Engineering, Accepted.
E. W. Remme, A. A. Young, K. F. Augenstein, P. J. Hunter

Paper E - The influence of material properties on left ventricular deformation in an elliptical model

Unpublished

E. W. Remme, P. J. Hunter

Chapter 1

Introduction

This thesis contains an introductory section and five separate papers. Each paper is self-contained with its own abstract and references. The first chapter of the introductory section presents the motivation and aims of the doctoral project together with the major contributions and a summary of the papers. A brief introduction to finite element modeling is given in chapter two together with a brief description of the myocardial microstructure. The introductory section is closed in chapter three with some concluding remarks and directions for further research.

1. 1 Motivation

Cardiovascular disease is the most common cause of death in Western society. According to Statistics Norway the disease accounted for 41% of the deaths in Norway in 2001 [1]. Thus, there is a huge interest in heart research. The research is carried out on all levels from genes, proteins, and cells to tissue and whole organ function. Alteration on one level will affect the above levels and ultimately change the pumping action of the heart. The opposite is also true; a change of the pumping conditions caused by e.g. a narrowed aortic valve might induce myocardial cell growth and cause myocardial hypertrophy as a compensatory mechanism to balance the increased ventricular pressure which usually follow such a disease [2].

Alterations of the heart wall motion may be used as an indicator of heart disease. The motion is sensitive to changes in both outside factors such as blood pressure and internal factors such as wall stiffness and myocardial oxygen supply. Clinically, it is common to look at images of heart motion to assess cardiac function and echocardiography is extensively used in hospitals. The images give a visual impression of the heart motion but the interpretation of the deformation is of a subjective nature. In the last decade tissue Doppler imaging and strain rate imaging has been introduced [3], [4] and provide more objective measures but the implementation of the new ultrasound techniques in clinical routine has been slow [5]. Magnetic resonance imaging (MRI) gives usually higher quality images compared to ultrasound but its clinical use is limited due to relatively high cost, longer acquisition times, the requirement for isolation from

radio frequency radiation, contraindications associated with MRI, and increased difficulty of patient intervention. MRI tissue tagging was developed during the late 1980s and throughout the 1990s [6]-[8] and is today the most accurate method for the non-invasive measurement of 3 dimensional (3D) heart wall motion and regional strain. However, it suffers from the same limitations as conventional MRI and currently the post-processing time to trace the tag lines through the whole cycle for all image slices takes from 1 to 2 days per subject. Recent developed techniques such as HARP (harmonic phase) look promising and may reduce the required investigation time [9], [10] and make the technique more clinically attractive.

The cardiac images provide valuable information about the state of the heart but even more information may be extracted from these measurements by combining them with mathematical models. Finite element (FE) models have been used together with MRI tissue tagging to extract strain information [8] and together with MRI as a tool for segmenting the left ventricular (LV) surfaces in the MR images [11].

The FE method is a powerful technique that is often used to calculate the strain and stress distribution in structures with complex geometry. FE models of the myocardium have evolved together with increased knowledge about the myocardial microstructure. During the 1990s the fiber-sheet structure of the myocardium and its orientation through the myocardial wall was thoroughly studied [12], [13]. The investigation revealed an orthotropic architecture of the myocardium with three distinct material axes: one along the fiber, one normal to the fibers but in the sheet, and one normal to the sheets (see chapter 2 for more on the microstructure). This discovery led to the development of a new orthotropic constitutive law (the pole-zero law) describing the stress-strain relationships in the three directions [14]. The FE method provides the framework for a mathematical description of both the geometry of the heart and the regionally varying microstructure of the myocardium [15], [14]. With appropriate boundary conditions applied to the FE model and inclusion of a constitutive law, simulations of the cardiac mechanics through the heart cycle can be carried out and provide information about for example the stress and strain distributions in the wall [14].

The applications of the FE method in heart research and in a clinical setting may be numerous. As a simulation model it can be used to test hypothesis and provide help to understand the function of various structures and parameters included in the model and their influence on the total heart function. A lot of effort is currently being put into the development of sophisticated gene and cell models and the incorporation of these models into an FE framework of the whole heart [16], [17]. Eventually this may for example make it possible to test the effects of drugs in a simulation model and reduce the requirements for animal testing [18]. In the clinic there is a huge demand for methods that can be used to estimate regional stresses and strains to assess the effects of disease and help in making a prognosis and operating decisions. It is not possible to measure regional stresses in the myocardium. Estimated fiber stress from simple force balance models based on rotational symmetry about the LV long axis may provide qualitative data that can be used in pressure and volume overloaded cases [19]. However, for regional disease states these approximations will not apply. Patient specific FE models may provide a more accurate method to calculate the stress and strain distribution in the myocardial wall. In principle the predicted behavior of the model is adjusted by optimizing the model parameters to measurements from the

patient. This requires the model to be so sophisticated that it behaves realistically compared with the measurements. At the same time the model must be so simple that it is possible to estimate the necessary parameters in the model (i.e. the parameters must be observable) to optimize its behavior with respect to the measurements.

1.2 Aims of the Study

The main aim of this project has been to develop methods that can extract more information on LV deformation from images of the heart by combining the images with an FE model of the LV.

Knowledge about the deformation of the LV is essential to assess LV function. Currently, MR tissue tagging is the most accurate method for the non-invasive measurement of 3D heart wall motion and regional strain. But the technique is not widely used due to its limitations. We thus wanted to develop a method that could estimate the LV deformation based on 3D anatomical images that were modality independent, i.e. the kind of images that could be obtained from other modalities such as echocardiography and computed tomography (CT) as well as standard MRI.

Quantification of the LV deformation is essential to be able to compare a subject's deformation with normal cases and other diseased cases. We wanted to develop a method that decomposed the deformation into different deformation modes such as longitudinal shortening, wall thickening, and twisting, and that quantified the relative contribution of each mode. The developed method would be validated on a group of normal subjects and their values compared with values obtained from a group of patients.

LV deformation is influenced by the material properties of the wall. Variations of the different parameters may have different effects on the various deformation modes. We wanted to increase our understanding of the relationship between the material parameters and the LV wall motion by simulating the deformation of an LV FE model and vary the material parameters to investigate corresponding changes in the deformation.

Calculation of mechanical stresses and strains in the LV myocardium by the FE method relies on adequate knowledge of the material properties of myocardial tissue. Results from *in vitro* stress-strain testing of myocardial tissue may be questionable as the tissue is disrupted and may be damaged. In addition it is not feasible to obtain tissue samples from human subjects. We wanted to develop a model-based estimation procedure based on cardiac images and blood pressure measurements to find the material properties and investigate the feasibility of such a method by analyzing the observability of the material parameters.

1.3 Contributions

The main contributions from this research project can be summarized as follows:

- The sensitivity of fiber, sheet, and sheet-normal strains of the myocardium to variations of the material parameters in the pole-zero constitutive law has been investigated. The results showed a high degree of coupling between the parameters within each direction. The sensitivity was generally smaller for the parameters in the sheet-normal direction than the fiber and sheet direction.
- A material parameter estimation routine was developed. It was only possible to estimate one parameter in each of the three microstructural directions due to observability problems. The estimated stress-strain relationships in the fiber and sheet directions were estimated well, while the estimated relationship in the sheet-normal direction was less accurate.
- A routine to estimate the LV deformation was developed and evaluated on 13 normal subjects. The method was based on tracing fiducial markers on the wall. An FE model was shaped to the geometry of the LV wall and the nodal parameters of the mesh were fitted to the motion of the fiducial markers.
- A method that decomposed the LV deformation into separate deformation modes was developed. Each mode was quantified by its mode coefficient. The method was evaluated on 13 normal subjects and 13 diabetes patients and their coefficient values compared.
- An investigation of the material parameters' influence on the deformation modes was carried out on an FE model of the LV. Different mesh motions were obtained by simulating the heart cycle from the inflation phase through to end ejection and using different material parameters.

1.4 Summary of Papers

Paper A - Ventricular mechanics in diastole: material parameter sensitivity

Paper A describes the development of a finite element model from measurements of the pig heart. The model took into account the anisotropic fiber and sheet structure of the myocardium and included inhomogeneous material properties. Using finite deformation theory and the non-linear pole-zero constitutive law, the end-diastolic deformation of the model was computed. The sensitivities of end-diastolic fiber-sheet material strains and heart shape to changes in the material parameters were computed for the parameters of the pole-zero law in order to assess the utility of the model for inverse material property determination.

Paper B - Development of an in vivo method for determining material properties of passive myocardium

The work presented in Paper B is an extension of the work done in the previous paper. A Gauss-Newton approach was implemented to estimate the material parameters of the pole-zero constitutive law based on measurements of LV wall strains. The method was tested on synthetic strain data obtained by simulating the LV inflation phase with known material parameters. In this way we were able to verify the correctness of the solution and investigate the influence of introduced measurement noise and model errors on the calculated values. An observability analysis showed that it was only possible to estimate one parameter in each of the three material directions. The estimated parameters in the fiber and sheet directions converged well for all tested magnitudes of noise while the estimated value of the parameter in the sheet-normal direction showed a higher degree of uncertainty. Thus, depending on how well the FE model represents the true LV, the results show that it may be possible to estimate the stress-strain relationship in the fiber and sheet direction.

Paper C - Parameter distribution models for estimation of left ventricular deformation using sparse fiducial markers

A method to estimate LV motion based on 3D images is presented in paper C. The method was developed independent of imaging modality, i.e. the images could be obtained from any anatomical tomographic or 3D modality, such as echocardiography, CT or MRI. A finite element mesh of the LV was constructed to fit the geometry of the wall. The mesh was deformed by optimizing the nodal parameters to the motion of a sparse number of fiducial markers that were manually tracked in the images through the cardiac cycle. The fiducial markers were distinct anatomical landmarks that could be

manually traced from frame to frame and included points such as the intersections of valves, papillary muscles and the right ventricular wall with the LV wall, and distinct trabecula structures on the endocardial surface. A parameter distribution model (PDM) of LV deformations was obtained from a database of MR tagging studies. This was used to filter the calculated deformation and incorporate *a priori* information on likely motions. The estimated deformation obtained from 13 normal untagged studies was compared with the deformation obtained from MR tagging. The end systolic (ES) circumferential and longitudinal strain values matched well with a mean difference of $0.1\pm 3.2\%$ and $-0.3\pm 3.0\%$, respectively. The calculated apex-base twist angle at ES had a mean difference of $1.0\pm 2.3^\circ$. We concluded that fiducial marker fitting in conjunction with a PDM provides accurate reconstruction of LV deformation in normal subjects.

Paper D – Extraction and quantification of left ventricular deformation modes

Paper D describes a developed method that decomposed the deformation of the LV into separate deformation modes such as longitudinal shortening, wall thickening, and twisting between end diastole (ED) and ES. The deformation was initially found from the motion of an LV finite element mesh that was fitted to clinically obtained MR tagged images. The deformation of the mesh between ED and ES was approximated as a sum of extracted deformation modes multiplied by their mode coefficients. The coefficients were calculated using a linear least-squares method. We applied the method to 13 normal subjects and 13 diabetes patients. By using the ED mesh as reference and adding to it the deformation modes multiplied by their coefficients, an approximate ES mesh was calculated and compared with the “true” ES mesh found from the MR images. For the 26 subjects the average Euclidean distance was 1.7 ± 0.9 mm between the nodes of the approximated and true ES mesh. The extracted modes showed a low degree of coupling and the calculated coefficients had low variance for the group of normal subjects. The coefficient values for the patient group showed significantly less longitudinal shortening, less wall thickening, more longitudinal twisting and also more bulging of the septum into the LV when compared with the normal subjects. In conclusion the developed method was capable of quantifying the deformation into several modes of deformation and distinguishing the deformation of a group of patients from a group of normal subjects.

Paper E - The influence of material properties on left ventricular deformation in an elliptical model

Paper E describes a study where the effect of variations of the material properties on LV deformation was investigated in a simulation model. An elliptically shaped FE model was used as an approximation to the LV wall geometry. The model incorporated a description of the varying myocardial fiber and sheet orientations through the wall together with a passive orthotropic constitutive law and a steady state active law that generated a stress component along the fibers during systole. The inflation phase, isovolumetric contraction phase, and ejection phase were simulated by applying appropriate boundary conditions on the model through the various phases. The deformation of the FE mesh that occurred between the ED mesh configuration (after the inflation phase) and the ES mesh (end ejection) was decomposed into different deformation modes such as wall thickening and longitudinal shortening using the method described in paper D. To investigate the effects of the material parameter values on the deformation modes, we repeated the simulation with varying material parameters. The result showed reduced wall thickening with stiffer passive properties along the fiber direction. Stiffer sheets resulted in a pronounced reduction of both wall thickening and longitudinal shortening. Changes of the sheet-normal stiffness had little effect on the modes except for moderately reduced longitudinal shortening for stiffer parameter values. Increased sheet - sheet-normal shear stiffness reduced wall thickening. The majority of the results were consistent with other studies and the variations in deformation modes could for the most part be interpreted in terms of myocardial microstructure and orientation.

Chapter 2

Introduction to the Finite Element Method

Piecewise approximation to difficult functions by using simple function over a limited range is a mathematical technique that has been used for several milleniums [20]. The FE method is one such technique that was developed during the middle of the last century and got its name when it was first applied to analyze structural frames in aircraft during the 1950s [20]. Since then the number of applications of the technique has increased rapidly and its increased use has followed hand in hand with the development of computational power as the method is computational expensive. The FE method and variations of it are described in numerous textbooks. This chapter is intended to give the readers with no FE knowledge a brief introduction to the method and describe some methods that are more specific to this project.

Many structures have too complex a geometry to find analytical solutions to the stress and stain distributions inside the structure when a load is applied to it. The basic idea behind the FE method is to discretize (segment) the structure into many elements, set up the equilibrium equations for all elements, and solve the equations in simultaneous fashion by means of matrices. The (field-) variables of the model are interpolated using a so-called basis function or just interpolation function. A one-dimensional element with length L in the x -direction is shown in Fig. 1 where the field value $u(x)$ is a variable that varies along the element. This field value could for example represent the y coordinate along the element line ($u=y$), i.e. the change of geometry along the x -direction, or u could represent the myocardial fiber angle that changes along a line through the heart wall. A linear interpolation of u is shown in (1) and illustrated with the dashed line as compared with the true function $u(x)$ represented with the solid line. The function $u(x)$ is sampled with discrete nodal values at each side of the element, u_1 and u_2 . The material element coordinate, $\xi=x/L$, represents the position inside the element from element node 1 ($\xi=0$) to element node 2 ($\xi=1$).

$$u(x) \approx \left(1 - \frac{x}{L}\right)u_1 + \frac{x}{L}u_2 = (1 - \xi)u_1 + \xi u_2 = \sum_{i=1}^2 \Psi_i(\xi)u_i \quad (1)$$

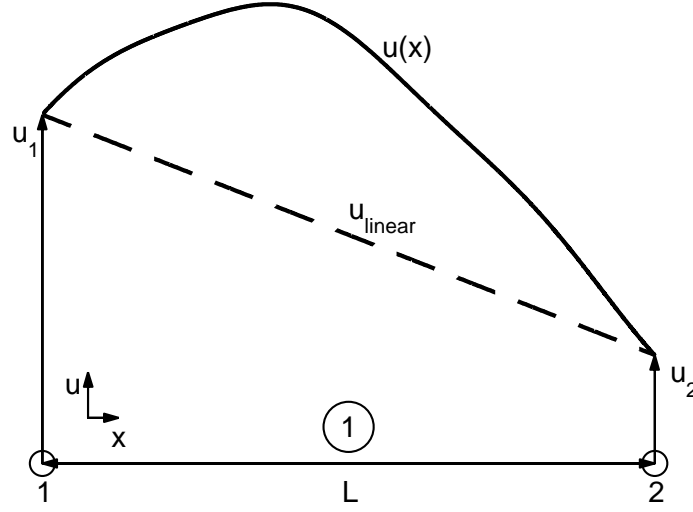


Figure 1. The function $u(x)$ is approximated by u_{linear} along a line in the x -direction using one element and linear interpolation. The values of function $u(x)$ at nodes 1 and 2 of element ① are u_1 and u_2 , respectively.

By refining the mesh, i.e. increase the discretization of the structure a better approximation may be obtained. This is shown in Fig. 2 for the same problem where the line is now represented by two elements. For each element the linear interpolation is carried out and the approximation is shown with the dashed line. Another way to improve the approximation to the true $u(x)$ is to introduce a higher order interpolation function. A cubic Hermite basis function is shown in (2). This requires the additional information about the derivatives of $u(x)$ at each node. The cubic Hermite basis function provide continuity in the first derivative with respect to arc length as opposed to the linear interpolation which has a discontinuous slope at the element boundaries (see the dashed versus the dotted line in Fig. 2). This property makes cubic Hermite basis functions well suited for representing smooth varying lines or surfaces such as the heart wall.

$$u(x) \approx \Psi_1^0(\xi)u_1 + \Psi_1^1(\xi)\left(\frac{du}{d\xi}\right)_1 + \Psi_2^0(\xi)u_2 + \Psi_2^1(\xi)\left(\frac{du}{d\xi}\right)_2$$

where

$$\Psi_1^0(\xi) = 1 - 3\xi^2 + 2\xi^3 \quad \Psi_2^0(\xi) = \xi^2(3 - 2\xi)$$

$$\Psi_1^1(\xi) = \xi(\xi - 1)^2 \quad \Psi_2^1(\xi) = \xi^2(\xi - 1)$$

(2)

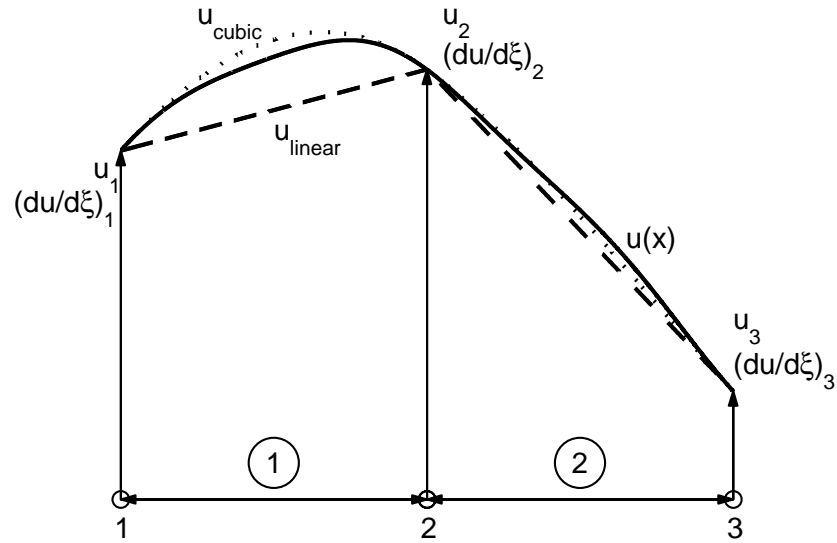


Figure 2. The function $u(x)$ is approximated using two elements. The dashed line (u_{linear}) represents a linear interpolation while the dotted line (u_{cubic}) is obtained by using cubic Hermite interpolation. The cubic Hermite interpolation requires the derivatives at each node which also make the slope of the interpolated function continuous.

Generalization of the FE method to 2 and 3 dimensions is fairly straightforward. A 2D element is represented by material coordinate ξ_1 along direction 1 and ξ_2 along direction 2, both varying between 0 and 1 from side to side. Equation (3) shows the interpolation of u using linear basis functions. Fig. 3 shows a geometric FE model of the LV wall using 3D elements that are cubic in the circumferential and longitudinal directions and linear through the wall.

$$u(x) \approx \sum_{i=1}^4 \Psi_i(\xi_1, \xi_2) u_i$$

where

$$\Psi_1(\xi_1, \xi_2) = (1 - \xi_1)(1 - \xi_2) \quad (3)$$

$$\Psi_2(\xi_1, \xi_2) = \xi_1(1 - \xi_2)$$

$$\Psi_3(\xi_1, \xi_2) = (1 - \xi_1)\xi_2$$

$$\Psi_4(\xi_1, \xi_2) = \xi_1\xi_2$$

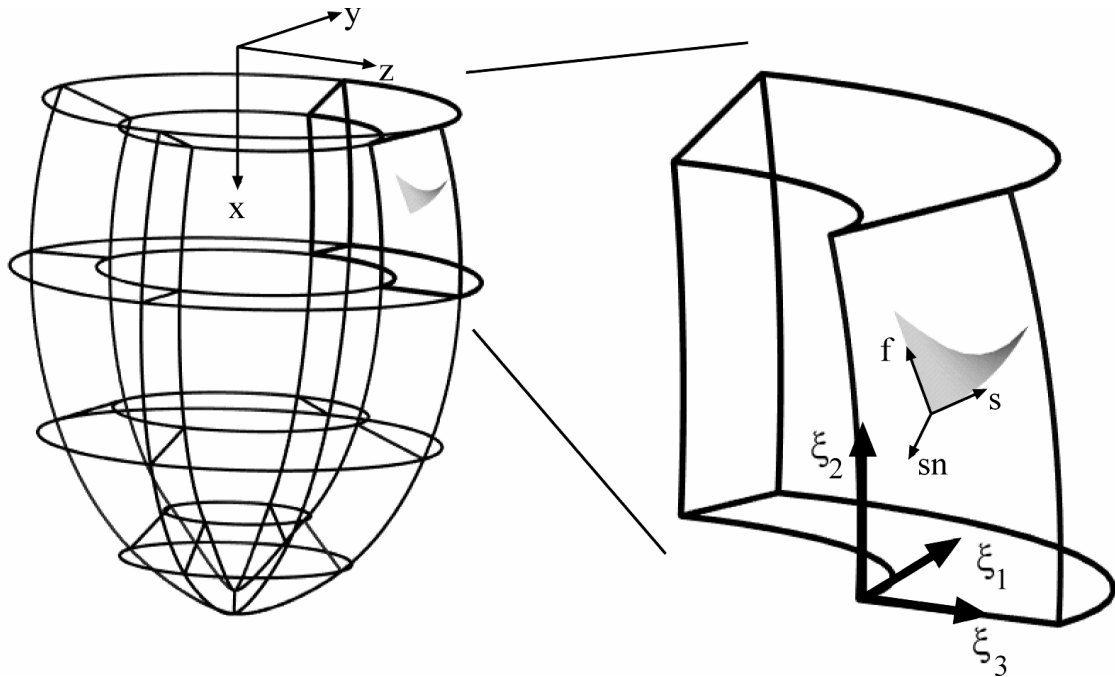


Figure 3. The figure shows a finite element mesh of a truncated ellipsoid as an approximation to the LV wall on the left and an enlargement of one element from this mesh on the right. The mesh is made up of 16 elements: 4 circumferential and 4 longitudinal. Cubic Hermite interpolation functions are used in the circumferential and longitudinal directions while linear interpolation is used through the wall. The global rectangular Cartesian coordinate system is shown on the left while the element (ξ_i) coordinates are shown for the element on the right where ξ_1 is in the circumferential direction, ξ_2 is in the longitudinal direction, and ξ_3 is in the radial direction. The figure also shows the microstructural material axes for cardiac tissue illustrated with a sheet of myocardial fibers inside the element. The microstructural axes are defined as f along the fibers, s along the sheet but perpendicular to the fibers, and sn along the sheet-normal. The microstructural axes are orthogonal in the undeformed configuration.

The FE model can incorporate a description of the material inside the mesh. In the case of myocardial tissue it has been found that the myocardial fiber angle varies through the wall. The fibers lie in ellipsoidal shells, parallel to the inner and outer surfaces and are mainly longitudinally oriented at the subendocardium, i.e. an angle of close to 90° with respect to the circumferential coordinate. The fiber angle rotates towards 0° in the mid-wall, i.e. circumferentially oriented, and rotates further to approximately -70° at the subepicardium [12]. Recent investigations have shown that the myocardial fibers are arranged in discrete layers or sheets approximately 3-4 cells thick, which are separated with so-called cleavage planes [13]. The fibers are bound by endomyial collagen within the sheet while the layers of sheet are relatively loosely connected together by perimyial collagen as shown in Fig. 4. Three material axes are thus evident: one along the fiber direction (fiber axis), one orthogonal to the fiber but in the sheet (sheet axis),

and one orthogonal to the sheets (sheet-normal axis). Also the orientation of the sheets varies locally within the wall. Fig. 3 shows how a sheet of fibers typically changes orientation in a small part of the wall. By using the FE interpolation techniques as described above, the regional variation of the fiber and sheet angles in the myocardial wall may thus be described.

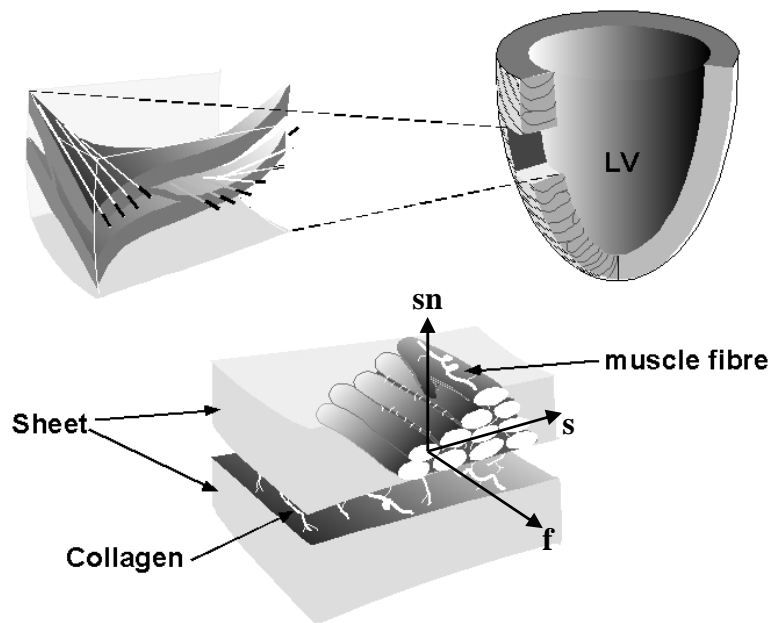


Figure 4. The figure shows a schematic of the fibrous-sheet structure of the cardiac tissue. A transmural segment (top left) from the ventricular wall is shown with fiber axis vectors embedded in the myocardial sheets, which are 3 to 4 cells thick, as shown in the lower figure. The fibers are tightly bound together in the sheet while the sheets are loosely connected. The axes in the lower figure indicate the three microstructural axes: f - fiber, s - sheet, and sn - sheet-normal. (Modified from [21].)

The inclusion of the myocardial microstructure and its regional varying orientation is important as the stress-strain relationships in the three material directions are different [22]. In addition active tension is only generated along the fiber direction during systole. The passive property is stiffest in the fiber and sheet direction and relatively much softer in the sheet-normal directions as shown in Fig 5. It is believed that the structure and material properties play a major role in the deformation of the heart wall during the cardiac cycle [23], [24].

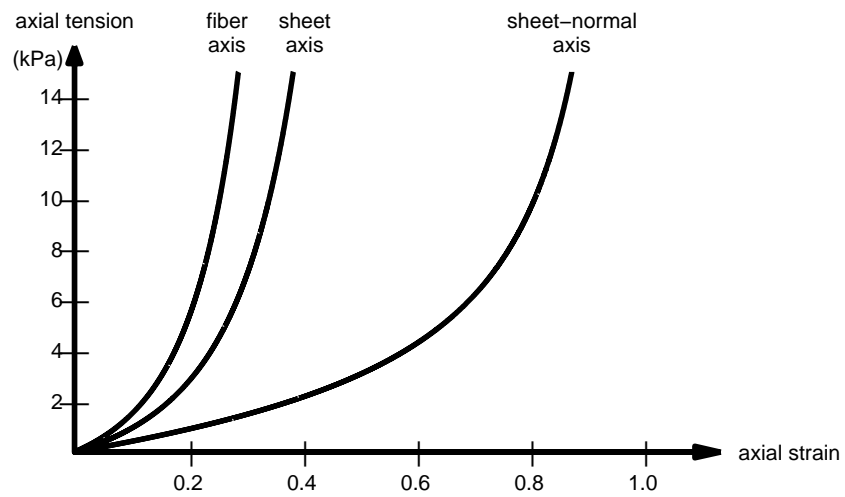


Figure 5. Stress-strain relationships in the three microstructural directions. The stiffness in the sheet-normal direction is relatively much softer than in the fiber and sheet directions as the sheets are loosely coupled together while the fibers are tightly bound by connective tissue within the sheets.

Chapter 3

Conclusions and Further Research

3.1 Conclusions

The main aim of this project has been to combine FE models of the LV with cardiac images to extract more information about LV deformation.

The FE method was chosen to model the LV as it provided the framework needed to describe the complex geometry of the LV including a description of the microstructure and to perform simulations of the deformation by including a material law and applying boundary conditions and loads.

We used the FE method to estimate the LV deformation by manually tracing the motion of fiducial markers on the LV wall in 3D images of the heart and fit the nodal parameters of the mesh to the motion of the markers. The number of fiducial markers was relatively small compared with the number of nodal parameters in the fitting procedure causing the solution to be under-constrained. A parameter distribution model (PDM) was constructed and provided *a priori* information on the probability distribution of possible LV motions. The probability distribution of motion was derived from a historical database of MR tissue tagging cases, previously analyzed with FE modeling. The calculated deformation was filtered via the PDM and the resulting deformation from 13 normal subjects using this technique compared well with the deformation obtained from MR tagged data.

LV deformation is influenced by cardiac disease. Different diseases may affect the deformation in different ways. Our method for decomposing the deformation into separate deformation modes and quantifying each mode may provide a method to investigate the effect of the disease and separate normal subjects from sick subjects. Ultimately, the method may provide some help in identifying different diseases. The disease is likely to influence the material properties of the myocardium. We performed a simulation study where an FE model of the LV was deformed by including the pole-zero constitutive law together with a model of the active fiber tension during systole and applying appropriate boundary conditions. Several simulations were carried out with varying material parameters. The mode analysis on the resulting deformed meshes

showed that stiffer fibers and particularly sheets impaired longitudinal shortening and wall thickening. An increase of the stiffness preventing shearing of the sheets also decreased wall thickening. These findings corresponded well with the measurements of Costa et al. [24] who found that the stretch of the sheets, which were mainly transmurally oriented, accounted for roughly half the wall thickening at ES as the fibers contract, while shearing of the sheets accounted for remainder part. The study that compared young normal subjects with older diabetes patients showed also a marked reduction of the wall thickening and longitudinal shortening in the patient group. That may indicate that the patients had stiffer myocardium than the normal group.

The sensitivity analysis of the end-diastolic strains to variations of the material parameter values showed a high degree of coupling of the parameters within each of the three material directions. This suggested an over-parameterization of the constitutive law. In the parameter estimation routine several of the parameters were set to constant values and only one parameter in each direction was estimated. This still gave good results for the stress-strain relationship in the fiber and sheet direction. The stiffness in the sheet-normal direction is considered to be much softer than in the two other directions due to the relatively looser binding of the sheets by the connective tissue. In the simulation it seemed like variation of the sheet-normal stiffness had little influence on the deformation which was probably limited by the stiffer fibers and sheets and this may have been the reason for the less accurate estimation of the sheet-normal stress-strain relationship. This was consistent with the deformation modes analysis which also showed minor influence on the deformation modes when the sheet-normal stiffness was varied.

3.2 Directions for Further Research

The over-parameterization of the pole-zero law was evident in the sensitivity analysis and estimation procedure. It is important to note that the pole-zero law was designed to represent the full range of elastic strain while the sensitivity analysis and parameter estimation routine were carried out during the diastasis phase and atrial contraction phase with only small LV pressure change and the resulting strains were small (usually < 10%). There may be other alternative constitutive laws that are better suited for *in vivo* parameter estimation with less coupled parameters. This is an area of active research [25] and new material laws are currently being developed.

It is quite common to use homogeneously distributed material parameters in FE models of the myocardium to reduce model complexity and also due to lack of knowledge about the regional variations of the connective tissue density and organization. Improved knowledge of the collagen distribution and organization may be obtained from microscopic mapping of the myocardial wall [26]. A new confocal microscope system has been built that is capable of imaging the myocardial microstructure at typically 1 μm resolution where layers of myocardial tissue are automatically imaged and shaved off in a repetitive fashion, see example in Fig. 6. It takes ~50 hours to scan a 700 μm \times 900 μm \times 3500 μm block from the LV wall at this resolution [27]. The long

acquisition time makes it infeasible to image the whole heart at this resolution but samples from several regions could give some indication to what extent regional variations of material properties should be implemented in an FE model of the normal heart.

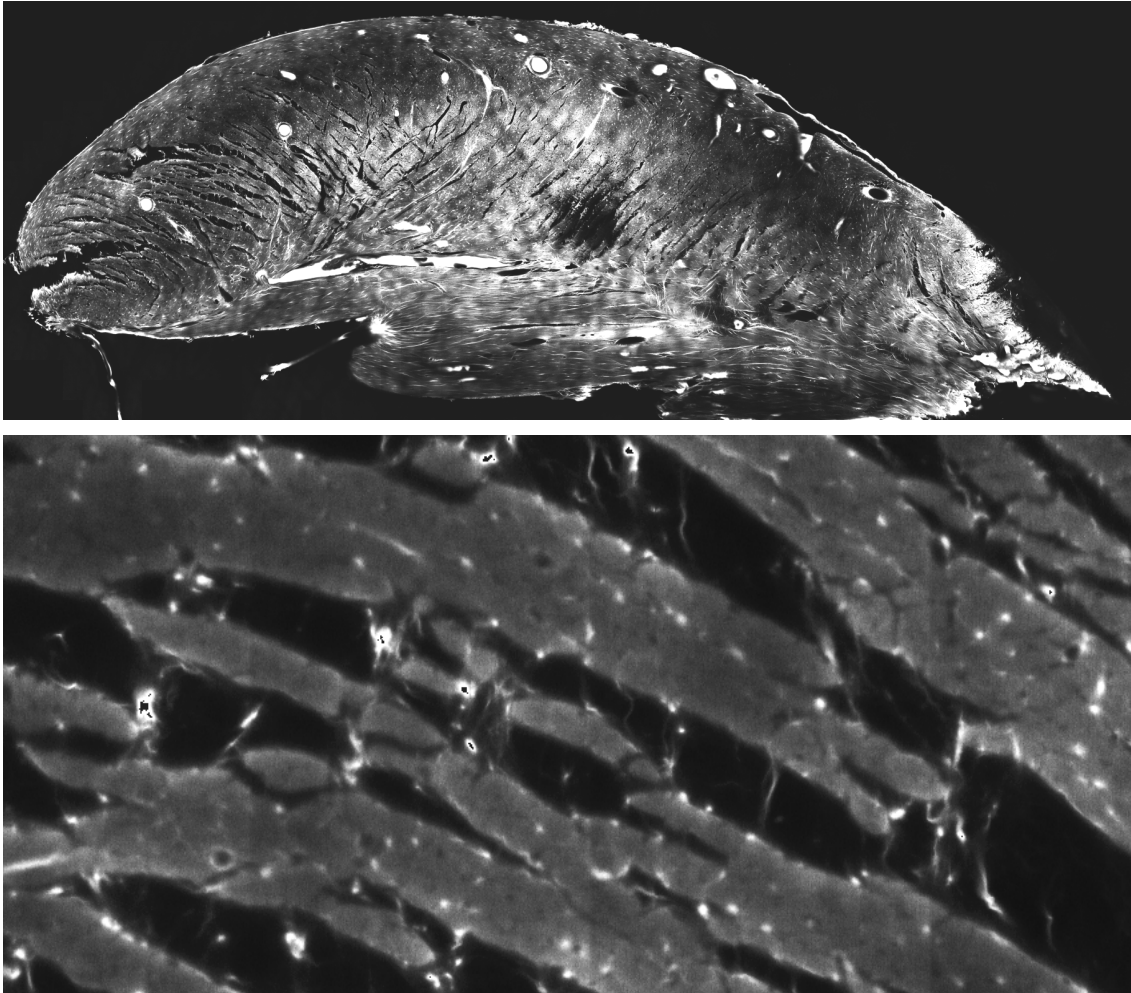


Figure 6. Images from the new confocal microscope system. The top image shows a $14.6 \text{ mm} \times 5.4 \text{ mm}$ longitudinal section of a rat LV myocardium obtained at $2 \mu\text{m}$ resolution. The bottom image shows a $850 \mu\text{m} \times 425 \mu\text{m}$ section obtained at $1 \mu\text{m}$ resolution. ©2003 Greg Sands and Ian LeGrice, Bioengineering Institute, University of Auckland, New Zealand. Images reprinted by permission.

This research project has mainly focused on the LV. The LV FE models did not take into account the influence from the right ventricle (RV). The pressure on the RV side of the septum and the intersection of the RV wall with the LV wall are likely to have significant impact on the LV deformation. A future development of the simulation models should include a model of the RV to correct for its influence on the LV. The pericardial sac and the atria are also likely to have some effect on the deformation and should be included in the modeling.

The effect of the papillary muscles is also missing. These are likely to have a significant influence on the deformation during systole when they contract and pull down on the mitral leaflets possibly contributing to the longitudinal shortening that occurs during this phase. There is also a growing interest for applying the FE method to study the mitral apparatus and investigate the strains and stresses in the papillary muscles, chordae tendinae, and mitral leaflets in relation to valve repair/replacement. Thus, we expect the papillary muscles to be included in the model as one of the first new developments of the model.

So far the interaction with the fluid has been represented with only a constant pressure on the endocardial surface of the FE mesh and as a constant volume constraint of the LV cavity during the isovolumic phases. It is known that significant pressure gradients develop in the LV during the ejection phase of the cardiac cycle (~10 mmHg from apex to base) [28]. This may have some effect on the deformation and the fluid-structure interaction should be investigated. From a fluid modeling perspective there is also a demand to develop a fluid-structure model as the blood flow is mainly controlled by the pumping action of the heart wall.

The simulated active fiber tension has been generated using a simple homogenous steady state law in this research work. Alternative active models are likely to be implemented in the near future. This includes a coupled electro-mechanical model, recently tested in 2D [29], where the propagation of the activation wave initiates the cell contraction that generates the active fiber tension. The Physiome project [30] is aimed at constructing a framework that makes exchanging biological models easier by the development of common standards through the use of open mark-up languages such as CellML [31]. The framework should make it easier to implement and test new constitutive laws both for passive and active myocardium. Thus, it is a goal to develop the current FE software so that it is capable of incorporating the models from this database with the possibility to couple various modules together and ultimately model the whole organ function of the heart.

References

- [1] Statistics Norway, (2003, June), "Dødsårsaker, 2001". Available: <http://www.ssb.no/emner/03/01/10/dodsarsak/>
- [2] A. M. Katz, *Heart failure. Pathophysiology, molecular biology, and clinical management*, Philadelphia, USA: Lippincott Williams & Wilkins, 2000, chap. 2.
- [3] A. Heimdahl, A. Støylen, H. Torp, T. Skjærpe, "Real-time strain rate imaging of the left ventricle by ultrasound," *J. Am. Soc. Echocardiogr.*, vol. 11, pp. 1013-1019, Nov. 1998.
- [4] S. Urheim, T. Edvardsen, H. Torp, B. Angelsen, O. A. Smiseth, "Myocardial strain by Doppler echocardiography. Validation of a new method to quantify regional myocardial function," *Circ.*, vol. 102, pp. 1158-1164, Sep. 2000.
- [5] O. A. Smiseth, H. Ihlen. "Strain rate imaging: why do we need it?" *J. Am. Coll. Cardiol.*, vol. 42, pp.1584-1586, Nov. 2003.
- [6] E. A. Zerhouni, D. M. Parish, W. J. Rogers, A. Yang, E. P. Shapiro, "Human heart: tagging with MR imaging-a method for noninvasive assessment of myocardial motion," *Radiology*, vol. 169, pp. 59-63, Oct. 1988.
- [7] L. Axel, L. Dougherty, "Heart wall motion: improved method of spatial modulation of magnetization for MR imaging," *Radiology*, vol. 172, pp. 349-350, Aug. 1989.
- [8] A. A. Young, D. L. Kraitchman, L. Dougherty, L. Axel, "Tracking and finite element analysis of stripe deformation in magnetic resonance tagging," *IEEE Trans. Med. Imaging*, vol. 14, pp. 413-421, Sep. 1995.
- [9] N. F. Osman, W. S. Kerwin, E. R. McVeigh, J. L. Prince, "Cardiac motion tracking using CINE harmonic phase (HARP) magnetic resonance imaging," *Magn. Reson. Med.* vol. 42, pp. 1048-1060, Dec. 1999.
- [10] D. L. Kraitchman, S. Sampath, E. Castillo, J. A. Derbyshire, R. C. Boston, D. A. Bluemke, B. L. Gerber, J. L. Prince, N. F. Osman, "Quantitative ischemia detection during cardiac magnetic resonance stress testing by use of FastHARP," *Circ.* vol. 107, pp. 2025-2030, Apr. 2003.
- [11] A. A. Young, B. R. Cowan, S. F. Thrupp, W. J. Hedley, L. J. Dell'Italia, "Left ventricular mass and volume: fast calculation with guide-point modeling on MR images," *Radiology*, vol. 216, pp. 597-602, Aug. 2000.

- [12] P. M. Nielsen, I. J. LeGrice, B. H. Smaill, P. J. Hunter, "Mathematical model of geometry and fibrous structure of the heart," *Am. J. Physiol.*, vol. 260, pp. H1365-H1378, Apr. 1991.
- [13] I. J. LeGrice, P. J. Hunter, B. H. Smaill, "Laminar structure of the heart: a mathematical model," *Am. J. Physiol.*, vol. 272, pp. H2466-2476, May 1997.
- [14] M. P. Nash, P. J. Hunter, "Computational mechanics of the heart: from tissue structure to ventricular function," *J. Elasticity*, vol. 61, pp. 113-141, 2000.
- [15] K. D. Costa, P. J. Hunter, J. S. Wayne, L. K. Waldman, J. M. Guccione, A. D. McCulloch, "A three-dimensional finite element method for large elastic deformations of ventricular myocardium: II-Prolate spheroidal coordinates," *J. Biomech. Eng.*, vol. 118, pp. 464-472, Nov. 1996.
- [16] D. Noble, "Modeling the heart from genes to cells to the whole organ," *Science*, vol. 295, pp. 1678-1682, Mar. 2002.
- [17] P. J. Hunter, T. K. Borg, "Integration from proteins to organs: the Physiome Project," *Nat. Rev. Mol. Cell Biol.*, vol. 4, pp. 237-243, Mar. 2003.
- [18] D. Noble, "The rise of computational biology," *Nat. Rev. Mol. Cell Biol.*, vol. 3, pp. 459-463, Jun. 2002.
- [19] S. I. Rabben, F. Irgens, B. Angelsen, "Equations for estimating muscle fiber stress in the left ventricular wall," *Heart Vessels*, vol. 14, pp. 189-196, 1999.
- [20] P. Allaire, *Basics of the Finite Element Method. Solid Mechanics, Heat Transfer, and Fluid Mechanics*, Iowa, USA: Wm. C. Brown Publishers, 1985, pp. 8.
- [21] I. J. Le Grice, B. H. Smaill, L. Z. Chai, S. G. Edgar, J. B. Gavin, P. J. Hunter, "Laminar structure of the heart: ventricular myocyte arrangement and connective tissue architecture in the dog," *Am. J. Phys.*, vol. 269, pp. H571-H582, Aug. 1995.
- [22] B. H. Smaill, P. J. Hunter, "Structure and function of the diastolic heart: Material properties of passive myocardium," in *Theory of heart: biomechanics, biophysics, and nonlinear dynamics of cardiac function*, L. Glass, P. J. Hunter, A. D. McCulloch, Eds. New York: Springer-Verlag, 1991, pp. 1-29.
- [23] I. J. LeGrice, Y. Takayama, J. W. Covell, "Transverse shear along myocardial cleavage planes provides a mechanism for normal systolic wall thickening," *Circ. Res.* vol. 77, pp. 182-93, Jul. 1995.
- [24] K. D. Costa, Y. Takayama, A. D. McCulloch, J. W. Covell, "Laminar fiber architecture and three-dimensional systolic mechanics in canine ventricular myocardium," *Am. J. Physiol.*, vol. 276, pp. H595-607, Feb. 1999.
- [25] J. C. Criscione, A. D. McCulloch, W. C. Hunter, "Constitutive framework optimized for myocardium and other high-strain, laminar materials with one fiber family," *J. Mech. Phys. Solids*, vol. 50, pp. 1681-1702, Aug. 2002.
- [26] A. A. Young, I. J. LeGrice, M. A. Young, B. H. Smaill, "Extended confocal microscopy of myocardial laminae and collagen network," *J. Microsc.*, vol. 192, pp. 139-150, Nov. 1998.

- [27] G. Sands, M. Trew, D. Hooks, I. LeGrice, A. Pullan, B. Smaill, "Constructing a tissue-specific model of ventricular microstructure," Proceedings of the 26th Annual International Conference of the IEEE Engineering in Medicine and Biology Society, San Francisco, Sep. 2004.
- [28] A. Pasipoularides, J. P. Murgu, J. W. Miller, W. E. Craig, "Nonobstructive left ventricular ejection pressure gradients in man," *Circ Res.*, vol. 61. pp. 220-227, Aug. 1987.
- [29] N. P. Smith, M. L. Buist, A. J. Pullan, "Altered T wave dynamics in a contracting cardiac model," *J. Cardiovasc. Electrophysiol.*, vol. 14, pp. S203-S209, Oct. 2003, Suppl.
- [30] <http://www.physiome.org.nz>
- [31] <http://www.cellml.org>

Paper A

Ventricular mechanics in diastole: material parameter sensitivity

Carey Stevens¹, Espen Remme^{1,2}, Ian LeGrice¹ and Peter Hunter¹

¹Bioengineering Institute, University of Auckland, New Zealand

²Department of Circulation and Medical Imaging, NTNU, Trondheim, Norway

Abstract

Models of ventricular mechanics have been developed over the last 20 years to include finite deformation theory, anisotropic and inhomogeneous material properties and an accurate representation of ventricular geometry. As computer performance and the computational efficiency of the models improve, clinical application of these heart mechanics models is becoming feasible. One such application is to estimate myocardial material properties by adjusting the constitutive parameters to match wall deformation from MRI or ultrasound measurements, together with a measurement (or estimate) of ventricular pressure. Pigs are now the principal large animal model for these studies and in this paper we present the development of a new three-dimensional finite element model of the heart based on measurements of the geometry and the fibre and sheet orientations of pig hearts. The end-diastolic deformation of the model is computed using the “pole-zero” constitutive law which we have previously used to model the mechanics of passive myocardial tissue specimens. The sensitivities of end-diastolic fibre-sheet material strains and heart shape to changes in the material parameters are computed for the parameters of the pole-zero law in order to assess the utility of the models for inverse material property determination.

Journal of Biomechanics, 36: 737-748, May 2003

1 Introduction

The mammalian heart has an asymmetric shape and an anisotropic and inhomogeneous tissue structure [1]. Three-dimensional finite element analysis is therefore essential for determining the stress and strain fields. Since material deformations during the cardiac cycle are large (fibre strains typically reach 10% at end-diastole), large deformation elasticity theory is required, with constitutive laws based on the anisotropic fibrous structure of myocardium. Fluid movement within the myocardium, especially within the subendocardium at end-systole, does cause some effective tissue compressibility but the assumption of an isochoric deformation (no volume change) is reasonable and is usually adopted [2].

The historical development of ventricular models is reviewed in [3]. Earlier models from the Auckland group [4], [5] have been based on prolate spheroidal coordinates for computational efficiency, but these models, which were based on measurements from canine hearts, did not accurately represent the geometry of the base and apex of the heart. With the availability of increased computational power we can now afford to use a more accurate model in rectangular Cartesian coordinates and fully tricubic Hermite basis functions. In this paper we present a new model of the left and right ventricles of the pig heart using rectangular Cartesian coordinates and using new measurements of geometry and of fibre and sheet orientations. A model of the passive properties of myocardial tissue, referred to material axes defined by the fibrous-sheet architecture, is used for computing the deformation, and hence the strain and stress fields, at end-diastole. The governing stress equilibrium equations, derived from large deformation elasticity theory, are reported in [2] and the pole-zero material constitutive law is described in [3].

2 Ventricular Geometry

The ventricular geometry and myocardial fibre angles of the heart of a 26 kg pig were measured in a manner similar to the earlier study performed on the canine heart [6] using a purpose built rig [7]. However, the design of the rig prevented accurate acquisition of the heart's base plane geometry because the probe approaches the base tangentially. Another three-dimensional digitisation device called a *FaroArm*¹ was therefore also used in the present study. The *FaroArm* is a multiple axis articulated arm with a rotary transducer on each joint and a spherical working volume. The coordinates of the probe tip are recorded with an accuracy of 75 μ m. The *FaroArm* was used to digitise the epicardial valve orifice geometry and the basal regions that were unreachable with the earlier rig.

To facilitate the combination of the two data sets three reference pins were inserted into the myocardium, two near the base in each ventricle's free wall, and the other near the apex. The pins' locations were digitised using both the rig and the *FaroArm*. A transformation matrix to rotate and translate the *FaroArm* data to align with the rig data

¹ Faro Technologies Inc. See <http://www.faro.com/>.

was computed using a nonlinear optimisation. The sum of the squared distances between the reference points in each data set was minimized to give a mean error of 0.2 mm.

The valve rings form the basis of the basal skeleton and the first step in creating the full ventricular model was to model the geometry of each of the valve annuli. One-dimensional cubic Hermite elements were fitted to the epicardial valve orifice data collected with the FaroArm (see [3] for a discussion of the cubic Hermite basis functions). The number of nodes and their initial positions were chosen to facilitate their inclusion in the full ventricular mesh. Fits of each of the fitted orifices are plotted in Fig. 1 and Table 1 lists the results of each fit. The degrees of freedom that described these elements were included as fixed parameters in the fitting of the ventricular surface meshes. The fitting procedures for the bicubic Hermite surface meshes are as described in [5]. The surface fit results are also given in Table 1.

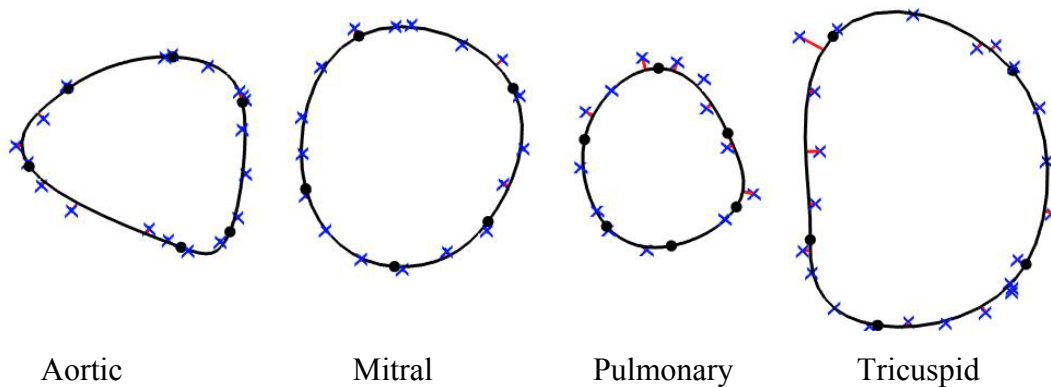


Figure 1. Heart valve rings shown in 2D projections. The ‘x’s are points measured with the Faro Arm and the solid lines and node points (•) show the fitted finite elements. The lines of projection of a data point onto the fitted elements are also shown.

Model	Nodes	Elements	Data Points	RMS Error (mm)
Mitral valve	5	5	17	0.47
Aortic valve	6	6	19	0.75
Tricuspid valve	5	5	23	0.83
Pulmonary valve	6	6	13	0.75
LV endocardial surface	56	54	888	0.93
RV endocardial surface	43	36	327	1.37
Epicardial surface	64	63	575	0.55

Table 1. Summary of valve orifice and surface fitting results.

A three-dimensional mesh was formed with tricubic Hermite basis functions in the three rectangular Cartesian coordinates and 79 elements. Creating a volume mesh from the three fitted surfaces required a consolidation of the common degrees of freedom and the introduction of new degrees of freedom to complete the transmural connections. Throughout the mesh construction process the nodal locations were chosen to ensure that the resultant volume elements are as near cuboid as possible. Multiple versions of the Hermite coordinate derivatives (see [3]) were used at a common node to connect the interventricular septum to the ventricular free walls. Geometrically equivalent derivatives in adjacent elements with inconsistent parametric coordinates (see Fig. 2b) were constrained to be the same, as were the corresponding elemental scale factors. C^1 continuity is not maintained across these element boundaries.

Another difference in mesh topology between the earlier dog heart model and the present pig heart model is shown in Fig. 2. Whereas the previous dog heart model had two elements through the wall, the present model has one. This simplification is possible because the element basis functions in the present model are tricubic Hermite, versus the previous bicubic-linear basis used for the dog heart. The present model also uses rectangular Cartesian coordinates, rather than the prolate spheroidal coordinates of the dog heart model.

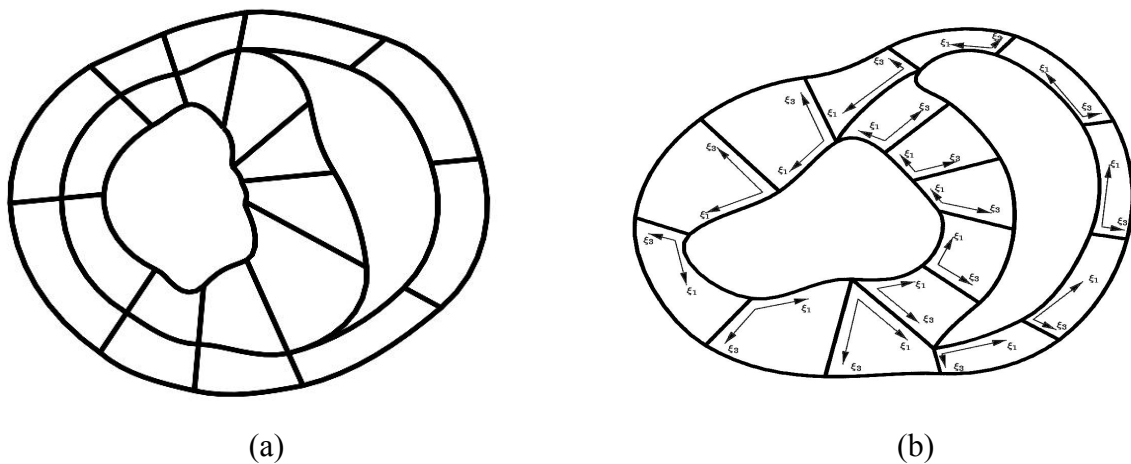


Figure 2. Crosssection of dog and pig heart models. (a) The previously published dog heart model [4] showing the cusp topology of the RV margins and the two element thick left ventricular free wall. (b) The new pig heart model with more rounded RV margins and one element thick walls throughout the model. The dog model used bicubic-linear elements with a prolate spheroidal coordinate system, whereas the new pig model uses tricubic Hermite elements in a rectangular Cartesian coordinate system. The vectors on this diagram show the orientation of the ξ_1 and ξ_3 parametric coordinates (ξ_2 is directed out of this plane).

The fitted three-dimensional pig heart mesh is shown in Fig. 3, where the valve orifices shown in planar projection in Fig. 1 can now be seen on the three-dimensional heart. Previous ventricular models have treated the apex as thick walled, similar to the rest of

the left ventricular (LV) free wall, but in reality the wall tapers steeply to a thin collagenous membrane. The fitted pig heart model now captures this anatomical detail, as shown in Fig. 3b. The fitted myocardial volume is 83.1 cc, the LV and right ventricular (RV) cavity volumes are 22.7 and 15.9 cc, respectively.

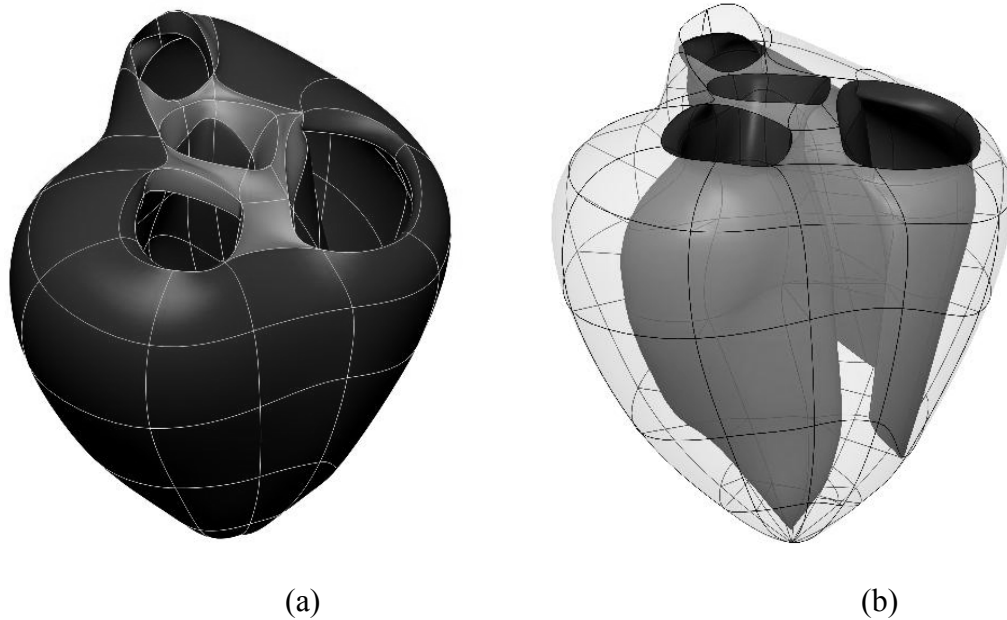


Figure 3. Fitted surfaces of pig heart model. (a) The epicardial surface of the 79 element finite element model of the right and left ventricles. Note that there are an additional 9 basal elements shown in this figure (but not in Fig. 3b), which are used to support heart valves but are not used in the simulations presented in this paper. (b) Endocardial surfaces of the left and right ventricles are seen through the translucent epicardial surface mesh. Note the very thin wall at the apex.

3 Myocardial Microstructure

The process of fitting the fibre field is described in [6]. The three-dimensional fibre field parameters were found by first fitting the LV endocardial, RV endocardial and epicardial surface fibre distributions using bicubic Hermite interpolation. With the longitudinal and circumferential surface parameters fixed, the transmural myocardial fibre angles were then fitted to measurements of fibre orientation throughout the myocardium. The transmural interpolation of the fibre field was also cubic Hermite, providing a tricubic Hermite representation of the fibre field.

There was little data to fit to around the base because the current measurement rig does not measure fibre angles accurately in the basal region. On the specimen it was observed that the fibres tend to continue in the same direction over the base to as they did along the wall. The application of Sobelov smoothing [8] enforced this constraint in the fit, providing a fibre field that resembled the observed fibre distribution about the

valve orifices well. A predominant fibre direction is not visible in the collagenous basal skeleton that connects the valve orifices. Therefore the fibre field was not fitted in the elements corresponding to the basal skeleton. The RMS errors for the fibre field fits are reported in Table 2. Fig. 4 shows the projection of the fibres onto a two-dimensional cross-section and Fig. 5 shows the fitted fibre fields at epicardial, midwall and endocardial locations.

Fibre Parameters	Number of Data Points	RMS Error
LV endocardium	622	0.27rad
RV endocardium	153	0.18rad
Epicardium	754	0.22rad
Transmural myocardium	4386	0.29rad

Table 2. RMS errors obtained in the fibre field fits.

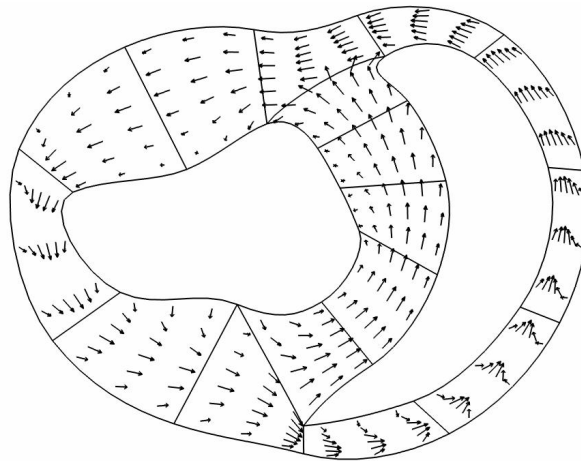


Figure 4. Fibre direction vectors projected onto a 2D cross-section of the pig heart model. All fibres are drawn as vectors with the same length, so the more axially aligned fibres in the subepicardium and subendocardium have a smaller projection onto this plane than the more circumferentially aligned midwall fibres. The apparent inward orientation of some of the subepicardial and subendocardial fibres reflects the taper of the wall (out of the plane of this projection) and does not indicate a non-zero imbrication angle. Notice the flow of fibres around the margins where the right ventricle joins the septum.

Cardiac tissue is composed of discrete layers of muscle fibres tightly bound by *endomysial* collagen and relatively loosely connected by *perimysial* collagen [6], as shown in Fig. 6. The layers, or “sheets”, can slide over one another with low shear resistance, a fact that facilitates the large wall thickening that occurs in systole [3]. To formulate a constitutive law for the mechanical properties of myocardial tissue, material axes are defined in the fibre direction (*fibre axis*), orthogonal to this in the plane of the sheets (*sheet axis*), and orthogonal to the sheets (*sheet-normal axis*).

The measurement and fitting of sheet angles is described in [6] although the protocol was modified to obtain optimal results for the pig hearts. The transformed sheet angle data was also fitted to 8360 data points using a tricubic Hermite field with an RMS error of 0.49rad. Cross-section plots of the fitted sheet fields are presented in Fig. 7.

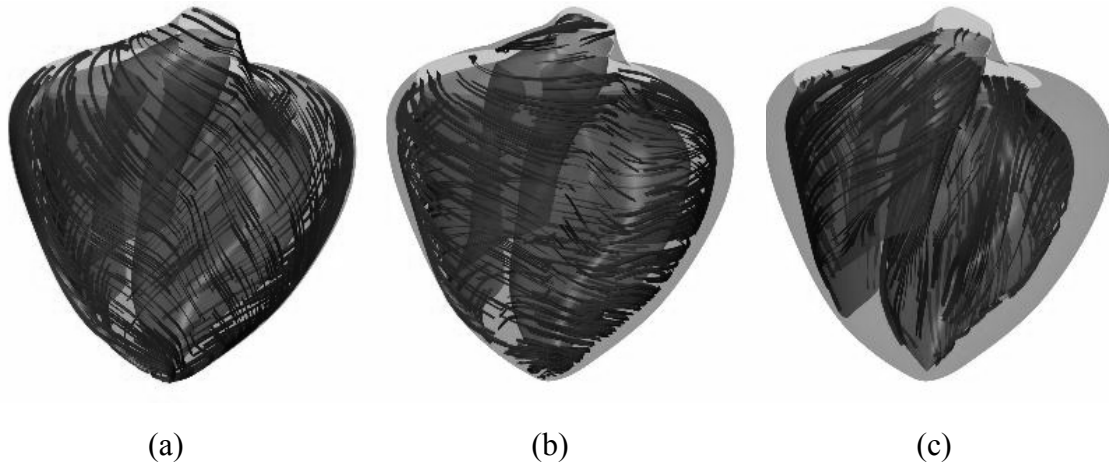


Figure 5. Muscle fibre orientations at three transmural depths: (a) epicardial, (b) midwall, and (c) endocardial. The fibre angle at the LV free wall (on the right in these figures) varies continuously from about -60° to the horizontal plane at the epicardium to $+80^\circ$ at the endocardium. The RV outflow tract is at the top centre in these figures.

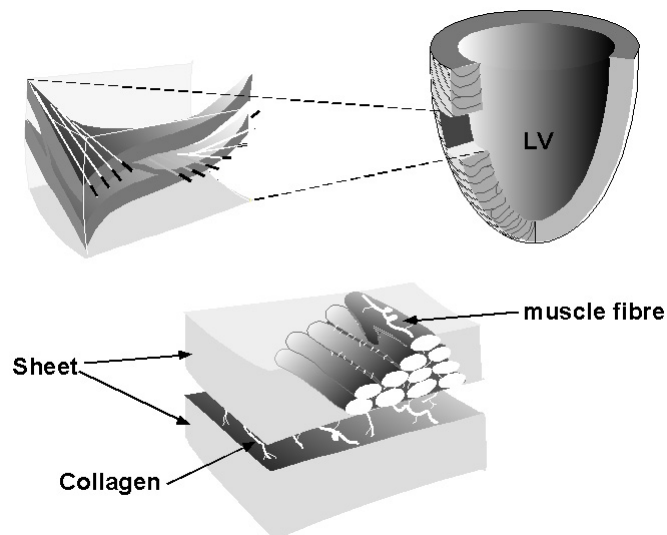


Figure 6. Schematic of fibrous-sheet structure of cardiac tissue. A transmural segment (top left) from the ventricular wall is shown with fibre axis vectors embedded in the myocardial sheets, which are 3 to 4 cells thick, as shown in lower figure. The myocytes are bound into the sheets with endomysial collagen and loosely connected with perimysial collagen. (Modified from [6].)



Figure 7. Fitted sheet orientations, shown in three longitudinal sections through the heart. Note the predominant radial orientation of the sheets. The apparent discontinuities in the plots are actually only an artefact of the rendering technique at element boundaries.

4 Myocardial material properties

When samples of myocardial tissue are loaded biaxially in the plane of the sheets or across the sheets, the stress along a material axis is almost independent of the strain along the other two axes. The stress-strain behaviour along any axis is highly nonlinear and is well represented by a strain energy term,

$$W = k \frac{e^2}{(a - e)^b}, \quad (1)$$

where the “pole” parameter ‘a’ represents the elastic limit for the strain component e , b is a corresponding exponent which determines the curvature of the stress-strain relation and k is a scale factor.

The assumption that the total strain energy is the sum of strain energy terms of the form (1) for all modes of deformation (3 axial and 3 shear), as given in Eq. 2, yields a good fit to stress-strain measurements in biaxial tests [7], [9] and shear tests [10] on myocardial tissue.

$$W = k_{11} \frac{e_{11}^2}{(a_{11} - e_{11})^{b_{11}}} + k_{22} \frac{e_{22}^2}{(a_{22} - e_{22})^{b_{22}}} + k_{33} \frac{e_{33}^2}{(a_{33} - e_{33})^{b_{33}}} \\ + k_{12} \frac{e_{12}^2}{(a_{12} - e_{12})^{b_{12}}} + k_{13} \frac{e_{13}^2}{(a_{13} - e_{13})^{b_{13}}} + k_{23} \frac{e_{23}^2}{(a_{23} - e_{23})^{b_{23}}} \quad (2)$$

The subscripts on the parameters in strain energy function denote the associated mode of deformation, 1 is in the fibre direction, 2 in the sheet direction and 3 is in the sheet-normal direction.

The parameter values used in the present study are given in Table 3. The stress-strain behaviour for each of the three material axes is shown in Fig. 8.

Type	Axial properties		Shear properties	
Coefficients	k_{11}	2.0 kPa	k_{12}	1.0 kPa
	k_{22}	2.0 kPa	k_{13}	1.0 kPa
	k_{33}	2.0 kPa	k_{23}	1.0 kPa
Poles	a_{11}	0.523	a_{12}	0.731
	a_{22}	0.681	a_{13}	0.731
	a_{33}	1.037	a_{23}	0.886
Curvatures	b_{11}	1.351	b_{12}	2.0
	b_{22}	1.351	b_{13}	2.0
	b_{33}	0.398	b_{23}	2.0

Table 3. Parameter values for the constitute law for passive myocardial tissue (Eq. 2).

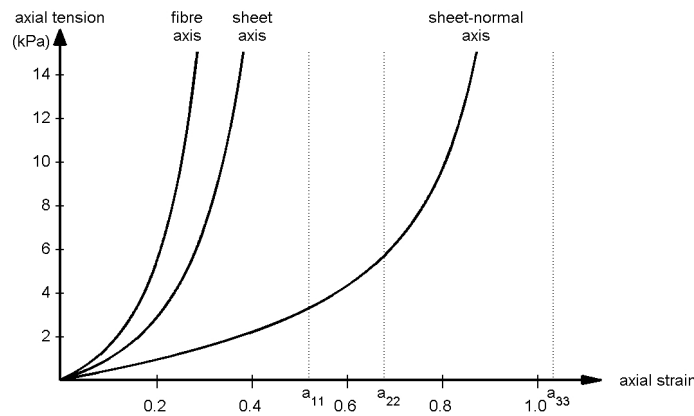


Figure 8. Stress-strain curves for each of the three material axes obtained from Eq. 2 with the material parameters given in Table 3. The pole values (a_{11} , a_{22} , a_{33}), representing the elastic strain limit, and therefore the asymptotes for these curves, are shown on the strain axis.

The ventricular wall in the absence of external loads is not completely stress free. Omens et al. [11] demonstrated this by radially cutting an equatorial cross-sectional ring and observing how it sprang open into an arc when the so-called residual stress was relieved. Several studies suggest that the residual stresses give rise to more uniform transmural distributions of end-diastolic myocardial stress [12]-[14]. The procedure for defining a growth tensor to accommodate these residual strain observations is described in [3]. Based on this data an initial trilinear fibre extension ratio field λ_{fi} was created to model the residual strain. In the equatorial region of the heart λ_{fi} varies from 0.95 on the LV endocardium and 1.0 on the RV endocardium to 1.05 on the epicardium. At the base and apex λ_{fi} is 1.0. To restore internal equilibrium within the ventricular myocardium the model is solved without any external loading.

5 Diastolic loading

In this section we examine the behaviour of the pig heart model under diastolic loading conditions. The finite element geometric model discussed above was used with Galerkin finite deformation stress analysis [3] and ventricular pressure boundary conditions to solve for deformed configuration of the model. All degrees of freedom at the base nodes were fixed and all degrees of freedom at all other nodes were free. The numerical integration of the element equations is performed with 3x3x3 point Gaussian quadrature. Since these “Gauss points” are the material points where the constitutive models are evaluated, we refer to these later when displaying the strain components. The model was inflated to a left ventricular (LV) pressure of 0.8 kPa and a right ventricular (RV) pressure of 0.16 kPa. The principal strain vectors at a number of points throughout the wall are shown in Fig. 9.

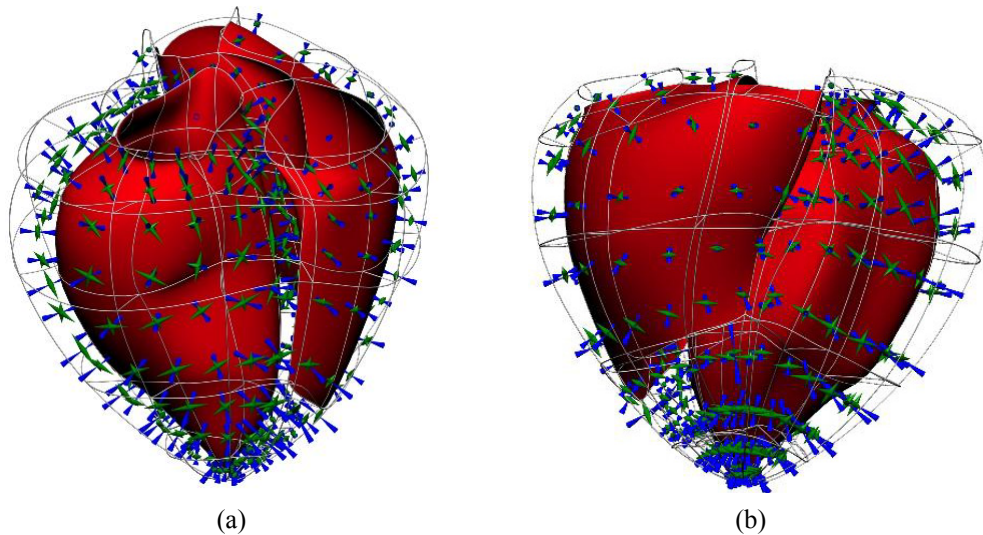


Figure 9. Principal strain vectors shown at end-diastole at midwall points of the finite element mesh. Green is tension and blue is compression. (a) Posterior view. (b) Anterior lateral view.

The normal material strain components along the fibre, sheet and sheet-normal directions are shown in Figs 10, 11 and 12 as extension ratios (stretches). Fig. 10 shows the fibre axis stretch at midwall locations around the LV with and without averaging in the base-apex direction (see Fig. 10 legend). These plots together with Fig. 12 show comparable spatial variation (about 0.05) of fibre stretch in the circumferential and base-apex directions. A major part of this circumferential variation can be attributed to the changing wall thickness. For example, the fibre strain peaks at the locations marked 10 and 11, which corresponds to the thinnest part of the wall. The low values of fibre strain at location 33 (and to lesser effect at location 3, 16 and 19) may be explained by the changing orientation of the fibres at the margins of the right ventricle as it merges with the left ventricle.

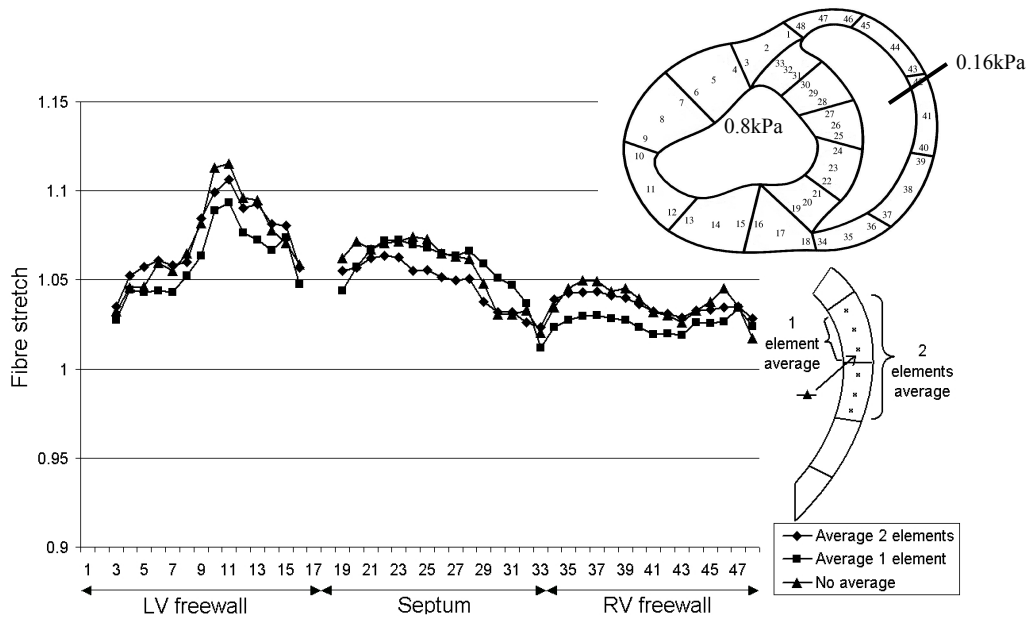


Figure 10. Circumferential distribution of fibre stretch at the midwall locations shown on the heart cross-section on the right. The numbers on the abscissa refer to Gauss point locations numbered in the sequence around the heart shown by the figure at the top right. Note that strain components at locations 1,2,17,18 are omitted because they do not lie on the LV circumferential path. Fibre stretch is plotted for no averaging (-▲-), averaged over 3 Gauss points in one element (-■-), and averaged over 6 Gauss points across two elements (-◆-), as indicated by the diagram on the right.

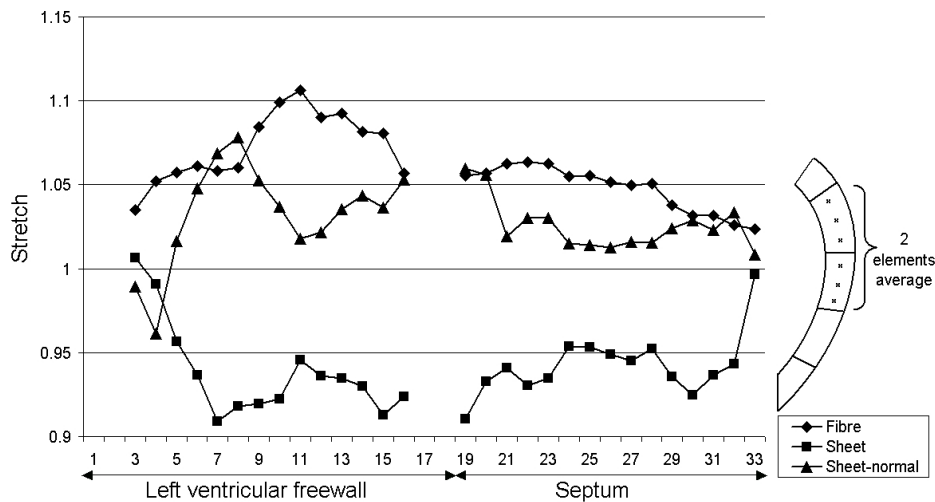


Figure 11. Mid-wall circumferential distributions of fibre (-◆-), sheet (-■-) and sheet-normal (-▲-) stretch, averaged over 6 Gauss points in two elements, as shown on diagram on the right. The numbers on the abscissa refer to the Gauss point locations indicated by the diagram at the top right in Fig. 10 (refer to the Fig. 10 legend for explanation of gaps in these plots).

The midwall circumferential distributions of fibre, sheet and sheet-normal stretch are shown in Fig. 11. These values have been obtained by averaging over 6 Gauss points (in the two elements indicated). The fibre stretch is the same plot as \blacklozenge in Fig. 10. The sheet stretch (\blacksquare) is <1 (except for the end point location 3 which is in the RV/LV junctional region) since the sheets are largely oriented in the radial and hence wall thinning direction. The sheet normal (\blacktriangle) is >1 (again with the exception of point 3); i.e. undergoing stretch, consistent with the elongation of the base-apex dimension of the heart during filling.

The distribution of fibre stretch along a base-apex path in the LV free wall is shown in Fig. 12 at subepicardial, midwall and subendocardial sites. These plots are obtained by averaging 6 circumferential Gauss points.

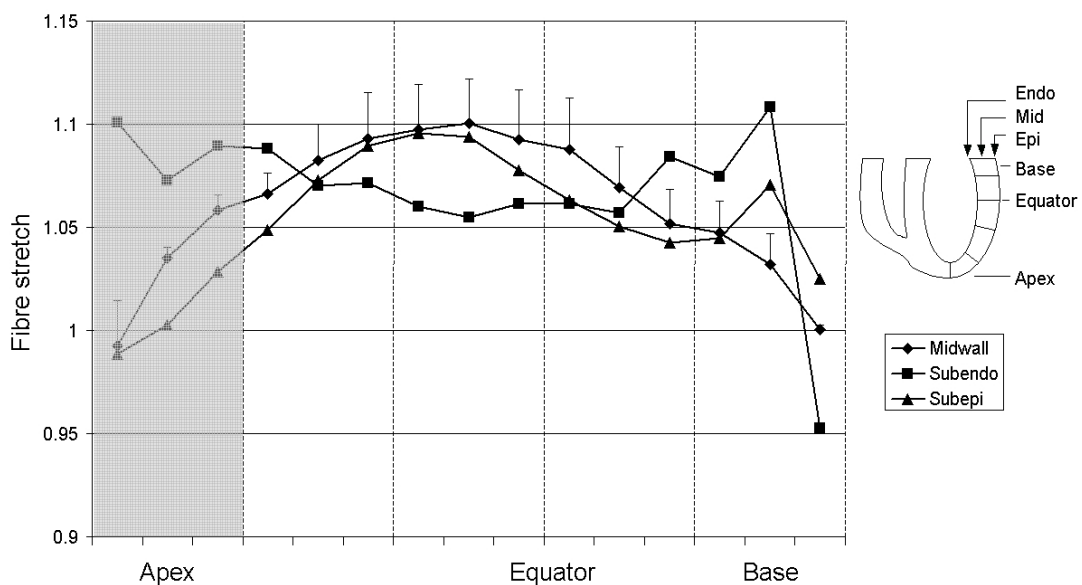


Figure 12. Distribution of fibre stretch along a base-apex path in the LV free wall at subepicardial (\blacktriangle), midwall (\blacklozenge) and subendocardial (\blacksquare) sites. The vertical divisions indicate element boundaries, as indicated in the schematic heart cross-section on the right. The apex region is shown shaded because the material properties in this ring of elements are chosen to yield a stiffer material than elsewhere (in order to achieve convergence of the model at high end-diastolic strain) and the strain results in this region reflect the stiffer material properties.

To confirm that a single transmural element is adequate to resolve the myocardial deformation, the LV free wall was refined transmurally. Both the original and the refined models were inflated to physiological end-diastolic LV and RV cavity pressures of 1.0 kPa and 0.2 kPa respectively. The end-diastolic Gauss point strain distributions for both models are plotted together for comparison in Fig. 13. The Gauss point strain comparisons between the original and the refined models indicate the original mesh is a suitable model for investigating myocardial deformation.

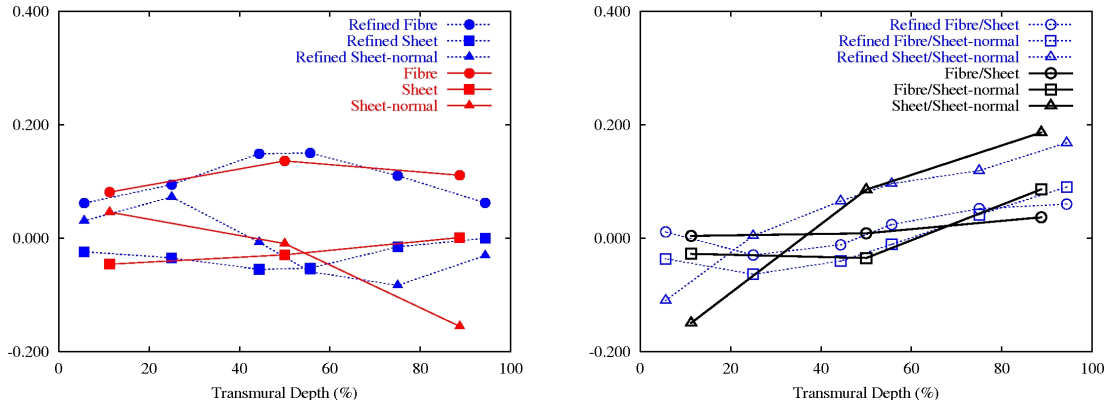


Figure 13. Transmurals Gauss point fibre strains at the equatorial lateral LV free wall at end-diastole for the original and the refined models. Refinement of the mesh yields little change in the predicted Gauss point strains.

Perturbed pole-zero law parameter	%Apex-base length change	%LV cavity volume change	%LV free wall thickness change	%Apex-base twist change
fibre pole +10%	0.20	2.52	-1.60	0.17
fibre pole -10%	-0.20	-2.60	1.60	0.12
sheet pole +10%	0.29	1.56	-0.82	0.08
sheet pole -10%	-0.35	-1.87	0.99	0.09
sheet-normal pole +10%	0.08	0.50	-0.21	0.03
sheet-normal pole -10%	-0.10	-0.60	0.25	0.04

Table 4. Sensitivity of global measures of ventricular function to changes in material parameters.

6 Material parameter sensitivity

An important long term clinical goal for the heart modelling is the determination of material parameters from models which have been fitted to tagged MRI clinical data [15]. As a step towards this goal we examine here the sensitivity of both the material strain components, and other more global measures of ventricular deformation (Table 4) at end-diastole, to changes in the material parameters.

6.1 Sensitivity analysis:

In order to assess the utility of the model for material property estimation, an analysis of the sensitivities of the end-diastolic fibre-sheet material strains to changes in the material parameters was performed. The calculated extension ratios at $N=918$ Gauss points were obtained from an inflation simulation with the set of $n=9$ axial material parameters, $\underline{\alpha}$, shown in Table 3. The calculated extension ratios were entered as the column vector \underline{y}_0 shown in Eq. 3.

$$\begin{array}{l}
 \text{Model response:} \\
 \underline{y}_0(\underline{\alpha}) = \begin{bmatrix} \lambda_{1-fibre} \\ \lambda_{1-sheet} \\ \lambda_{1-sheet\ normal} \\ \lambda_{2-fibre} \\ \vdots \\ \lambda_{918-sheet\ normal} \end{bmatrix} \\
 \end{array}
 \quad
 \begin{array}{l}
 \text{Parameters:} \\
 \underline{\alpha} = \begin{bmatrix} k_{11} \\ a_{11} \\ b_{11} \\ \vdots \\ b_{33} \end{bmatrix} = \begin{bmatrix} \alpha_1 \\ \alpha_2 \\ \alpha_3 \\ \vdots \\ \alpha_9 \end{bmatrix}
 \end{array}
 \quad (3)$$

The first parameter, α_1 , was then increased by 5% and another inflation simulation was solved with this perturbed parameter and the others kept at their original values. The result was entered in column vector \underline{y}_1 . Then parameter α_2 was increased by 5% and the others, including α_1 , were kept at their original values. The result from this simulation was entered in vector \underline{y}_2 . The procedure was repeated for all the parameters in $\underline{\alpha}$ resulting in vectors \underline{y}_1 to \underline{y}_9 .

To find the sensitivity of the model response to a variation in each parameter we looked at the norm of the column vector $(\underline{y}_m - \underline{y}_0)$. In this way it was possible to study the influence on the model response of a change of one parameter and to compare the sensitivity values of the different parameters. If a change of one parameter makes little difference on the model response, it will be difficult to estimate this parameter and the parameter's influence on the deformation may be minor. Table 5 shows the sensitivity values averaged for a change of the parameter values of +5% and -5%.

k_{11}	a_{11}	b_{11}	k_{22}	a_{22}	b_{22}	k_{33}	a_{33}	b_{33}
0.0651	0.1201	0.0788	0.0838	0.1162	0.0437	0.0437	0.0359	0.0022

Table 5. Sensitivity values. The values are the norm of the end-diastolic material axis extension ratio increments (evaluated at the Gauss points) resulting from a 5% increment in the indicated material parameters.

The variation of one parameter may cause a similar change in the model response as a variation of another parameter. To check this correlating behaviour a sensitivity matrix $S^T S$ was calculated. This was obtained by first calculating the matrix S shown in Eq. 4. The first column of S was calculated as $(\underline{y}_1 - \underline{y}_0) / \Delta\alpha_1$, the second column as $(\underline{y}_2 - \underline{y}_0) / \Delta\alpha_2$, and so on.

$$S = \frac{\partial \underline{y}}{\partial \underline{\alpha}} = \begin{bmatrix} \frac{\partial y_1}{\partial \alpha_1} & \frac{\partial y_1}{\partial \alpha_2} & \dots & \frac{\partial y_1}{\partial \alpha_n} \\ \frac{\partial y_2}{\partial \alpha_1} & \frac{\partial y_2}{\partial \alpha_2} & \dots & \frac{\partial y_2}{\partial \alpha_n} \\ \vdots & \vdots & \ddots & \vdots \\ \frac{\partial y_N}{\partial \alpha_1} & \frac{\partial y_N}{\partial \alpha_2} & \dots & \frac{\partial y_N}{\partial \alpha_n} \end{bmatrix} \quad \text{where } \underline{y} = \begin{bmatrix} y_1 \\ y_2 \\ \vdots \\ y_N \end{bmatrix} \quad (4)$$

Each column in S was normalised with respect to its norm creating the matrix \hat{S} and the sensitivity matrix $\hat{S}^T \hat{S}$. The elements in the sensitivity matrix express the correlation between the various parameters' influence on the model response, i.e. a value close to ± 1 for element \hat{S}_{ij} means that the parameters i and j are highly correlated. Table 6 shows the sensitivity matrix averaged for a +5% and -5% change of the parameter values.

	k_{11}	a_{11}	b_{11}	k_{22}	a_{22}	b_{22}	k_{33}	a_{33}	b_{33}
k_{11}	1.00	-0.97	0.99	0.55	-0.66	0.55	0.49	-0.48	0.39
a_{11}	-0.97	1.00	-0.98	-0.52	0.64	-0.52	-0.48	0.48	-0.40
b_{11}	0.99	-0.98	1.00	0.53	-0.64	0.54	0.48	-0.47	0.38
k_{22}	0.55	-0.52	0.53	1.00	-0.89	0.99	0.34	-0.06	0.42
a_{22}	-0.66	0.64	-0.64	-0.89	1.00	-0.89	-0.44	0.42	-0.45
b_{22}	0.55	-0.52	0.54	0.99	-0.89	1.00	0.34	-0.06	0.42
k_{33}	0.49	-0.48	0.48	0.34	-0.44	0.34	1.00	-0.74	0.63
a_{33}	-0.48	0.48	-0.47	-0.06	0.42	-0.06	-0.74	1.00	-0.45
b_{33}	0.39	-0.40	0.38	0.42	-0.45	0.42	0.63	-0.45	1.00

Table 6. Sensitivity matrix for a model response which includes all 3 material axis extension ratios at all 918 Gauss points.

An investigation of the separate sensitivities of the individual fibre, sheet, and sheet-normal strains to changes in the material parameters was also performed. There are now three output model response vectors as shown in Eq. 5.

$$\begin{array}{l}
 \text{Fibre response:} \\
 \underline{y} = \begin{bmatrix} \lambda_{1-fibre} \\ \lambda_{2-fibre} \\ \vdots \\ \lambda_{918-fibre} \end{bmatrix}
 \end{array}
 \quad
 \begin{array}{l}
 \text{Sheet response:} \\
 \underline{y} = \begin{bmatrix} \lambda_{1-sheet} \\ \lambda_{2-sheet} \\ \vdots \\ \lambda_{918-sheet} \end{bmatrix}
 \end{array}
 \quad
 \begin{array}{l}
 \text{Sheet-normal response:} \\
 \underline{y} = \begin{bmatrix} \lambda_{1-sheet normal} \\ \lambda_{2-sheet normal} \\ \vdots \\ \lambda_{918-sheet normal} \end{bmatrix}
 \end{array}
 \tag{5}$$

The result is three separate tables of sensitivity values and sensitivity matrices. The sensitivity values are given in Table 7. The correlations were qualitatively the same as the ones shown in Table 6.

Strain direction	k_{11}	a_{11}	b_{11}	k_{22}	a_{22}	b_{22}	k_{33}	a_{33}	b_{33}
Fibre	0.0439	0.0802	0.0534	0.0207	0.0483	0.0109	0.0104	0.0150	0.0005
Sheet	0.0371	0.0653	0.0446	0.0672	0.0866	0.0351	0.0220	0.0171	0.0012
Sheet-normal	0.0307	0.0610	0.0370	0.0455	0.0605	0.0236	0.0363	0.0278	0.0018

Table 7. The individual fibre, sheet, and sheet-normal sensitivity values when the model response is separated into fibre, sheet, and sheet-normal end-diastolic extension ratios, respectively.

7 Discussion

A new finite element mechanics model of the left and right ventricular myocardium has been developed. In contrast to an earlier prolate spheroidal model of the dog heart, the model is developed in rectangular Cartesian coordinates and uses tricubic Hermite basis functions for the geometric coordinates. The fibrous-sheet structure of the pig heart was measured and fitted with parameters defined at the nodes of the finite element mesh. In comparison with the earlier dog heart model, this new pig heart model gives a much more accurate description of the base and valve ring geometry. The thin apex of the heart is also now modelled more accurately than in the previous model. The papillary muscles, however, are not yet modelled - an important omission that needs to be rectified in the future because the mechanical loads transmitted from the systolically loaded mitral valve to the apical free wall by the papillary muscles is an important aspect of ventricular mechanics in systole (but not for the diastolic mechanics investigated here).

The model of the fibrous-sheet structure of the heart presented here assumes that the fibres lie in planes tangent to the epicardial and endocardial surfaces. From our measurements the out-of-plane deviation (imbrication angle) is less than 5deg for the bulk of the myocardium but is substantially greater than this for the regions of the myocardium close to the apex and base, where fibres spiral inward to provide continuity from epicardium to endocardium.

The material properties of the passive myocardium are represented here by the "pole-zero" constitutive equation, whose parameters have been obtained from biaxial testing of myocardial sheets. The constitutive equation is referred to material axes which are aligned with the fibre, sheet and sheet-normal directions defined by the finite element model. Transmural variations of material properties are not included in the model presented here.

The model of ventricular mechanics defined by the geometric finite element model, with the pole-zero constitutive law referred to the spatially varying fibre-sheet axes, is inflated with left ventricular and right ventricular pressures (0.8 kPa and 0.16 kPa, respectively) in order to obtain the stress and strain distributions at end-diastole. The circumferential distribution of fibre stretch (Fig. 10) reflects the circumferentially varying wall thickness. The peak fibre strain occurs between the regions where the free wall is thickened by the bulge of the papillary muscles. The minimum fibre strain occurs where the wall is thickest at the junction of the right ventricle with the septum.

Sheet strains are compressive (Fig. 11) because the sheets lie primarily in the transmural direction which thins during diastole. The sheet-normal direction is primarily in the base-apex direction and this is extended during diastole, yielding a positive sheet-normal stretch. The longitudinal distribution of fibre stretch (Fig. 12) is fairly uniform (within 5%, except at the base and apex) and with small transmural variations (also less than 5%).

An important clinical application of the finite element mechanics model will be to identify material parameters from kinematic measurements (e.g. from tagged-MRI or ultrasound imaging) together with direct or indirect measurements of ventricular pressure. In a preliminary investigation of this clinical goal we have examined the sensitivity of material strain measures to the parameters of the pole-zero constitutive model. The dominant result is in fact the large degree to which the parameters are coupled - primarily through the incompressibility constraint. This may indicate that the constitutive law needs to be reformulated to attempt a better separation of material parameters associated with dilatational and deviatoric stresses. The recent papers by Criscione et al. [16], [17] are a promising development and when the technique has been extended to orthotropic materials (as needed for myocardium) it can be tested with the parameter sensitivity techniques described here.

Acknowledgements

We would like to acknowledge the expert technical assistance of Jenny Hunter and Dane Gerneke for their help with the anatomical measurements on the pig hearts.

References

- [1] I. LeGrice, P. Hunter, A. Young, B. Smaill, "The architecture of the heart: a data-based model," *Philos. Transact. Ser. A Math. Phys. Eng. Sci.*, vol. 359, pp. 1217-1232, Jun. 2001.
- [2] K. D. Costa, P. J. Hunter, J. S. Wayne, L. K. Waldman, J. M. Guccione, A. D. McCulloch, "A three-dimensional finite element method for large elastic deformations of ventricular myocardium: Part II – Prolate spherical coordinates," *J. Biomech. Eng.*, vol 118, pp. 464-472, Nov. 1996.
- [3] M. P. Nash, P. J. Hunter, "Computational mechanics of the heart: from tissue structure to ventricular function," *J. Elasticity*, vol. 61, pp. 113-141, 2000..
- [4] P. M. F. Nielsen, I. J. Le Grice, B. H. Smaill, P. J. Hunter, "A mathematical model of the geometry and fibrous structure of the heart," *Am. J. Phys.*, vol. 260, pp. H1365-H1378, Apr. 1991.
- [5] I. J. LeGrice, P. J. Hunter, B. H. Smaill, "Laminar structure of the heart: a mathematical model," *Am. J. Physiol.*, vol. 272, pp. H2466-H2476, May 1997.
- [6] I. J. Le Grice, B. H. Smaill, L. Z. Chai, S. G. Edgar, J. B. Gavin, P. J. Hunter, "Laminar structure of the heart: ventricular myocyte arrangement and connective tissue architecture in the dog," *Am. J. Phys.*, vol. 269, pp. H571-H582, Aug. 1995.
- [7] P. M. F. Nielsen, P. J. Hunter, B. H. Smaill, "Biaxial testing of membrane biomaterials: Testing equipment and procedures," *J. Biomech. Eng.*, vol. 113, pp. 295-300, Aug. 1991.

- [8] A. A. Young, P. J. Hunter, B. H. Smaill, "Estimation of epicardial strain using the motions of coronary bifurcations in biplane cineangiography," *IEEE Trans. Biomed. Eng.*, vol. 39, pp. 526-531, May 1992.
- [9] B. H. Smaill, P. J. Hunter, "Structure and function of the diastolic heart: Material properties of passive myocardium," in: *Theory of heart: biomechanics, biophysics, and nonlinear dynamics of cardiac function*, L. Glass, P. J. Hunter, A. D. McCulloch, Eds., New York: Springer-Verlag, 1991, pp. 1-29.
- [10] S. Dokos, B. H. Smaill, A. A. Young, I. J. LeGrice, "Shear properties of passive ventricular myocardium," *Am. J. Physiol.*, vol. 283, pp. H2650-H2659, Dec. 2002.
- [11] J. H. Omens, Y. C. Fung, "Residual strain in the rat left ventricle," *Circulation Research*. Vol. 66, pp. 37-45, 1990.
- [12] J. M. Guccione, A. D. McCulloch, L. K. Waldman, "Passive material properties of intact ventricular myocardium determined from a cylindrical model," *J. Biomech. Eng.*, vol. 113, pp. 42-55, Feb. 1991.
- [13] E. K. Rodriguez, A. Hoger, A. D. McCulloch, "Stress-dependent finite growth in soft elastic tissue," *J. Biomech.*, vol. 27, pp. 455-467, 1994.
- [14] E. Nevo, Y. Lanir, "The effect of residual strain on the diastolic function of the left ventricle as predicted by a structural model," *J. Biomech.*, vol. 27, pp. 1433-1446, Dec. 1994.
- [15] K. F. Augenstein, E. R. McVeigh, A. A. Young, "Magnetic resonance imaging and ventricle mechanics," *Philos. Transact. Ser. A Math. Phys. Eng. Sci.*, vol. 359, pp. 1263-1275, Jun. 2001.
- [16] J. C. Criscione, J. D. Humphrey, A. S. Douglas, W. C. Hunter, "An invariant basis for natural strain which yields orthogonal stress response terms in isotropic hyperelasticity," *J. Mech. Phys. Solids*, vol. 48, pp. 2445-2465, 2000.
- [17] J. C. Criscione, A. S. Douglas, W. C. Hunter "Physically based strain invariant set for materials exhibiting transversely isotropic behaviour," *J. Mech. Phys. Solids*, vol. 49, pp. 871-897, 2001.

Paper B

Development of an *in vivo* method for determining material properties of passive myocardium

Espen W. Remme,¹ Peter J. Hunter,² Otto Smiseth,³ Carey Stevens,² Stein Inge Rabben,³ Helge Skulstad,³ Bjørn Angelsen¹

¹Department of Circulation and Medical Imaging, NTNU, Trondheim, Norway

²Bioengineering Institute, University of Auckland, New Zealand

³Institute for Surgical Research and Department of Cardiology, Rikshospitalet University Hospital, Oslo, Norway

Abstract

Calculation of mechanical stresses and strains in the left ventricular (LV) myocardium by the finite element (FE) method relies on adequate knowledge of the material properties of myocardial tissue. In this paper we present a model-based estimation procedure to characterize the stress-strain relationship in passive LV myocardium. A 3D FE model of the LV myocardium was used, which included morphological fiber and sheet structure and a nonlinear orthotropic constitutive law with different stiffness in the fiber, sheet, and sheet-normal directions. The estimation method was based on measured wall strains. We analyzed the method's ability to estimate the material parameters by generating a set of synthetic strain data by simulating the LV inflation phase with known material parameters. In this way we were able to verify the correctness of the solution and to analyze the effects of measurement and model error on the solution accuracy and stability. A sensitivity analysis was performed to investigate the observability of the material parameters and to determine which parameters to estimate. The results showed a high degree of coupling between the parameters governing the stiffness in each direction. Thus, only one parameter in each of the three directions was estimated. For the tested magnitudes of added noise and introduced model errors, the resulting estimated stress-strain characteristics in the fiber and sheet directions converged with good accuracy to the known relationship. The sheet-normal stress-strain relationship had a higher degree of uncertainty as more noise was added and model error was introduced.

1 Introduction

Finite element based continuum models of the heart, incorporating a detailed description of myocardial structure, are now frequently used to calculate stress and strain distributions. The major limitation of the predictive accuracy of these models is uncertainties about the best functional form of the constitutive law and the lack of knowledge of the specific law parameters.

In vitro stress-strain testing of myocardial tissue has been used to determine material parameters in the constitutive law [1]-[3]. The results from *in vitro* tests, however, may be questionable as the tissue is disrupted and may be damaged. From human subjects it is not feasible to obtain tissue samples. Moulton et al. [4], [5] developed an *in vivo* method for determining material properties by fitting a 2D FE model to strain measurements from magnetic resonance imaging (MRI) tagging. They were able to estimate the two material parameters of an isotropic, nonlinear, small deformation 2D FE model.

Detailed investigations of the myocardial structure [6], [7] have revealed that the myocardial fibers are arranged in layers or sheets. Based on *in vitro* biaxial stress-strain experiments [1], Hunter [8] proposed an orthotropic “pole-zero” constitutive law describing the different stress-strain relationships in the fiber, sheet, and sheet-normal directions. A 3D FE model of the LV myocardium that includes a description of the morphological fiber and sheet structures and uses the pole-zero constitutive law based on finite deformation theory will give more realistic deformation patterns than the model of Moulton et al. [4], [5]. However, the “pole-zero” constitutive law contains 18 material parameters but some are coupled via a micro-structural model [9]. A parameter estimation technique depends on the *observability* of the model parameters. If a perturbation of one parameter causes a similar model response to the perturbation of another parameter, then there might be poor observability, which makes the parameter estimation difficult. Stevens et al. [10] presented a sensitivity analysis of the material parameters that may be used to assess the observability.

The aims of this study were 1) to present a method for estimation of passive myocardial material parameters using the 3D FE model of Costa et al. [11] and Nash and Hunter [9], which is based on finite deformation theory and includes the myocardial fiber and sheet orientation and an orthotropic constitutive law, and 2) to investigate the feasibility of such a method by performing an observability analysis of the model parameters and checking the solution accuracy and stability with respect to introduced measurement and model error.

The final goal of a material estimation procedure like this is to combine the 3D FE model with strain measurements from for example MRI tagging. However, to investigate the feasibility of the method it is not necessary to include real strain measurements from MRI tagging. It is better to generate a synthetic test data set from a simulated inflation of the 3D FE model with known material parameters. By applying the material estimation procedure on the synthetic test data we can verify the correctness of the solution, investigate estimation stability, and assess the effects of

measurement and model errors. For the generation of the test data, the geometry of the FE model should be based on physiological measurements of the inner and outer surfaces of the heart. In this study the inner and outer surfaces were measured with 3D ultrasound.

2 Methods

2.1 Measurements

3D ultrasound measurements from four open-chest adult mongrel dogs were used to generate the test data. The study was approved by the National Animal Experimentation Board. Simultaneous measurements of the LV geometry and blood pressure were obtained. The pressure was measured using a 5F micromanometer-tipped catheter (model MPC-500, Millar Instruments, Houston, TX, USA) positioned in the LV. A Vivid FiVe ultrasound scanner (GE Vingmed Ultrasound) with a 3.5-MHz probe was used for the imaging. This system enables 3D/4D data acquisition based on a collection of 2D images. The probe is placed in a rotation adapter that rotates the probe 180° around the central axis of the imaging plane resulting in a conical data set. Apical 2D images were obtained over one heart cycle from 15 scan-planes distributed over the 180° rotation. The image file was later imported to a software program, EchoPac-3D (GE Vingmed Ultrasound), for post-processing. In this program contours were manually drawn around the endocardium and epicardium for all 15 scan-planes at the time of minimum LV pressure, which approximately corresponds to the beginning of the diastases.

2.2 The Finite Element Method

An initial finite element mesh was fitted to the measured geometry as described in [12] using the prolate spheroidal coordinate system shown in Fig. 1.

Investigations of the myocardial structure [6], [7] have revealed that the myocardial fibers are arranged in layers or sheets with three distinct material axes: one along the fiber direction, one orthogonal to the fiber direction but in the sheet, and one normal to the sheet. Following LeGrice et al. [13] the fiber angle was set to vary linearly from 85° at the endocardial surface to -60° at the epicardial surface. For the LV free-wall the sheet angle was set to vary linearly from -45° at the endocardial surface to +45° at the epicardial surface with respect to the radial coordinate. For the septum the sheet angle was set to vary linearly from +45° at the LV side to -45° on the RV side. The imbrication angle (the out-of-plane angle) of the fibers was set to zero.

In vitro biaxial stress-strain experiments on myocardial tissue samples have shown that the stress-strain behavior along the fiber, sheet, and sheet-normal directions is quite different [7]. On the basis of these experiments Hunter [8] proposed a strain energy function called the “pole-zero” law, equation (1), to describe the stress-strain relationship in the myocardium.

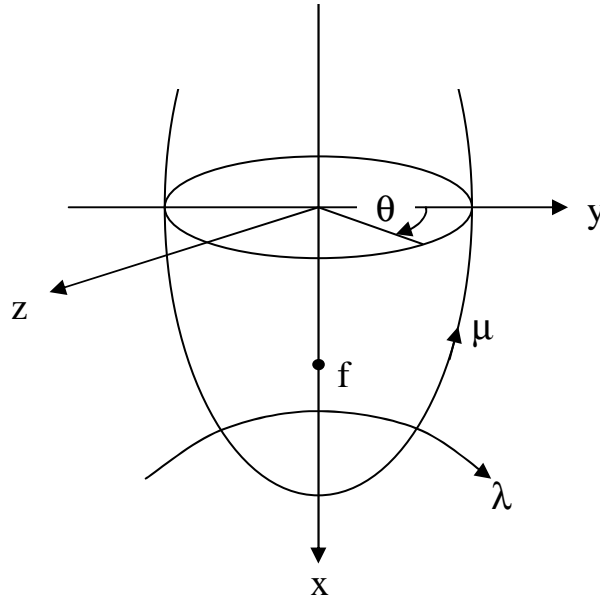


Figure 1. Prolate spheroidal coordinates: θ - circumferential, μ - longitudinal, λ - transmural, and focus f .

$$\begin{aligned}
 W = & k_1 \frac{e_{11}^2}{(a_1 - e_{11})^{b_1}} + k_2 \frac{e_{22}^2}{(a_2 - e_{22})^{b_2}} + k_3 \frac{e_{33}^2}{(a_3 - e_{33})^{b_3}} \\
 & + k_4 \frac{e_{12}^2}{(a_4 - e_{12})^{b_4}} + k_5 \frac{e_{13}^2}{(a_5 - e_{13})^{b_5}} + k_6 \frac{e_{23}^2}{(a_6 - e_{23})^{b_6}}
 \end{aligned} \tag{1}$$

In equation (1) index 1 refers to the fiber direction, index 2 refers to the sheet direction, and index 3 refers to the sheet-normal direction. e_{ij} are the covariant components of Green's strain tensor referred to these axes. (Note that these are physical components of strain because they are referred at each point to normalized orthogonal rectangular coordinates.) Indexes 11, 22, and 33 refer to longitudinal strains in the respective directions. The shear terms have indexes 12, 13, and 23. There are three different types of parameters in the constitutive equation: a_i are the poles or the limiting strains, b_i are related to the curvature of the uniaxial stress-strain relationships, and k_i are the relative weights of each term to the total strain energy. The components of the 2nd Piola-Kirchhoff stress tensor are derived from the strain energy function in equation (2) for the assumed incompressible material. p is the hydrostatic pressure and C is the Cauchy-Green deformation tensor.

$$T^{ij} = -p(C^{-1})^{ij} + \frac{1}{2} \left(\frac{\partial W}{\partial e_{ij}} + \frac{\partial W}{\partial e_{ji}} \right) \tag{2}$$

Note that, in the terminology of [9], the C^{-1} term is identical to the contravariant components a^{ij} of the deformed metric tensor for the material coordinates and the strain

components are given by $e_{ij} = \frac{1}{2}(a_{ij} - A_{ij})$, where a_{ij} and A_{ij} are the covariant components of the deformed and undeformed metric tensors, respectively.

Fig. 2 shows the three axial stress-strain curves for the pole-zero law using the parameters in Table 1. The stress-strain relationships in the three directions are clearly different: it is stiffest in the fiber direction, less stiff in the sheet direction normal to the fibers, and it is relatively much softer in the direction normal to the sheets. For negative strains, linear stress-strain relationships were used where the slopes for the negative strains were equal to the slopes of the pole-zero law at zero strain.

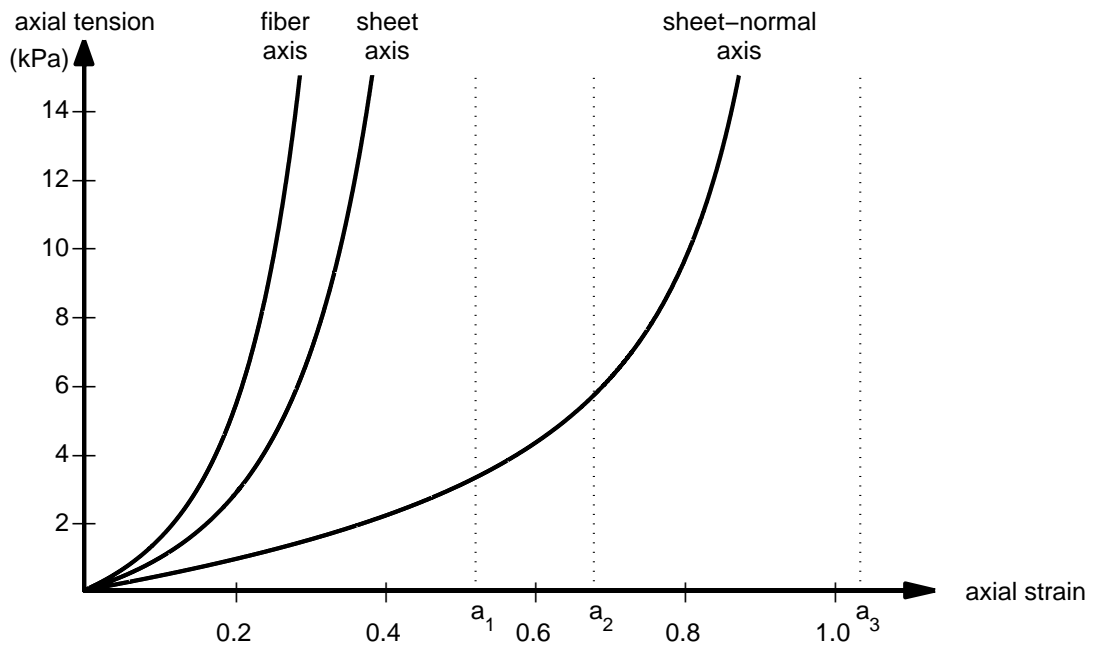


Figure 2. Stress-strain relationships calculated from the pole-zero law (equation 1) using the parameters in Table 1. The asymptotes on the strain axis are the poles (a_1, a_2, a_3) representing the elastic strain limits.

Nash and Hunter [9] showed that the shear poles in equation (1) were related to the axial poles as shown in equation (3). The other 6 shear parameters were set to constant values, leaving the 9 axial parameters to be estimated.

$$a_i = \frac{2a_j}{\sqrt{1+2a_j}}, \text{ when } \begin{matrix} i = 4, & a_j = \min(a_1, a_2) \\ i = 5, & a_j = \min(a_1, a_3) \\ i = 6, & a_j = \min(a_2, a_3) \end{matrix} \quad (3)$$

Residual strains [14] in the fiber direction were included in the reference configuration using the method of Rodriguez et al. [15]. The residual fiber strains varied linearly with a 5% stretch at the epicardium and a 2% contraction at the endocardium [16]. We assumed that the myocardium was in its most stress-free state at the beginning of the

B-6

diastasis. Thus, the geometric reference configuration was fitted to the contours drawn in the ultrasound images at the beginning of the diastasis.

During the inflation of the LV certain boundary conditions were imposed on the FE mesh. The epicardial apex node was fixed in the μ and θ directions. The base and apical nodes were fixed in the μ direction, and the epicardial base nodes were fixed in the θ direction.

Type	Axial properties		Shear properties	
Coefficients	k_1	2.0 kPa	k_4	1.0 kPa
	k_2	2.0 kPa	k_5	1.0 kPa
	k_3	2.0 kPa	k_6	1.0 kPa
Poles	a_1	0.523	a_4	0.731
	a_2	0.681	a_5	0.731
	a_3	1.037	a_6	0.886
Curvatures	b_1	1.351	b_4	2.0
	b_2	1.351	b_5	2.0
	b_3	0.398	b_6	2.0

Table 1. Material parameters used in the model. The parameter values in this table are referred to as the “true parameter values” in the text.

2.3 Generation of Test Data

In this study we wanted to develop and check the feasibility of a method for determining the stress-strain characteristic of passive myocardium. In order to analyze the method’s ability to estimate the material parameters we generated a set of synthetic strain data (in the following called the “test data”) by simulating the LV inflation phase with known material parameters (called the “true parameters”) listed in Table 1 [10]. By applying the material estimation procedure on the synthetic test data we can verify the solution, investigate estimation stability, and assess the effects of measurement and model errors.

To generate the test data we averaged the node coordinates of the geometric FE models of the four dog hearts. With the boundary conditions and the residual strains set, a passive inflation of the LV was simulated. This was done by applying the measured pressure difference of 0.4 kPa (average of the four dogs) between beginning of diastasis and end diastole on the endocardial element-surfaces of the LV. The simulated inflation was initially done with the true parameters. Circumferential, longitudinal and radial wall strains, or rather the extension ratios, λ_i , were written out and saved as the test data at 240 points around the LV (20 points circumferentially, 12 longitudinally and 1 radially), giving a total of $N=720$ extension ratio samples. In a clinical study the generated test data would be replaced by measured strains from, for example, MRI tagging.

2.4 Parameter Estimation

The estimation procedure was started with an initial guess of the parameter values different from the true parameter values. An iterative estimation process updated the material parameters as a function of the difference between the calculated extension ratios and the test data. When the solution had converged, the iteration process was stopped. The result after the final iteration contained an estimate of the material parameters. A block diagram of the algorithm is shown in Fig. 3.

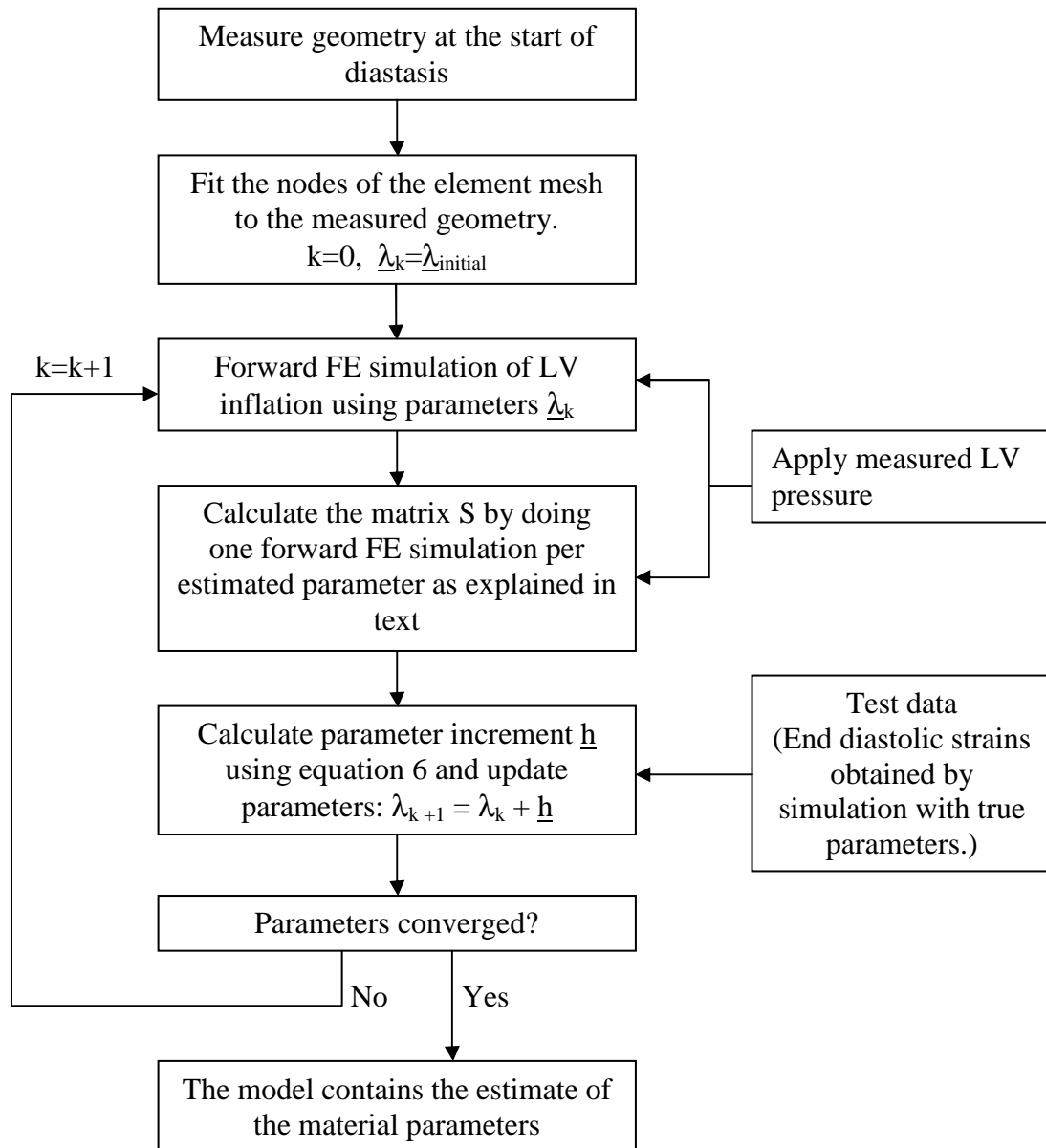


Figure 3. Flow diagram of the material property estimation procedure.

B-8

The material parameters, $\underline{\alpha}$, were estimated by minimizing the least-squares difference between the extension ratios, λ_i , of the test data and the extension ratios, $\hat{\lambda}_i$, of the model response:

$$J(\underline{\alpha}) = \frac{1}{2} [\hat{\underline{\Lambda}}(\underline{\alpha}) - \underline{\Lambda}]^T [\hat{\underline{\Lambda}}(\underline{\alpha}) - \underline{\Lambda}] \quad (4)$$

Model response:

Test data :

Parameters :

$$\hat{\underline{\Lambda}}(\underline{\alpha}) = \begin{bmatrix} \hat{\lambda}_1 \\ \hat{\lambda}_2 \\ \vdots \\ \hat{\lambda}_{720} \end{bmatrix} \quad \underline{\Lambda} = \begin{bmatrix} \lambda_1 \\ \lambda_2 \\ \vdots \\ \lambda_{720} \end{bmatrix} \quad \underline{\alpha} = \begin{bmatrix} k_1 \\ a_1 \\ b_1 \\ \vdots \\ b_3 \end{bmatrix} = \begin{bmatrix} \alpha_1 \\ \alpha_2 \\ \alpha_3 \\ \vdots \\ \alpha_9 \end{bmatrix} \quad (5)$$

An improved estimate of $\underline{\alpha}$ is obtained by adding an increment \underline{h} that decreases the error of the model response. The increment \underline{h} is found as shown in equation (6) and (7) by using the Gauss-Newton method to minimize the least-squares function in equation (4).

$$\underline{h} = (S^T S)^{-1} S^T (\underline{\Lambda} - \hat{\underline{\Lambda}}(\underline{\alpha})) \quad (6)$$

$$S = \frac{\partial \hat{\underline{\Lambda}}}{\partial \underline{\alpha}} = \begin{bmatrix} \frac{\partial \hat{\lambda}_1}{\partial \alpha_1} & \frac{\partial \hat{\lambda}_1}{\partial \alpha_2} & \cdots & \frac{\partial \hat{\lambda}_1}{\partial \alpha_n} \\ \frac{\partial \hat{\lambda}_2}{\partial \alpha_1} & \frac{\partial \hat{\lambda}_2}{\partial \alpha_2} & \cdots & \frac{\partial \hat{\lambda}_2}{\partial \alpha_n} \\ \vdots & \vdots & \ddots & \vdots \\ \frac{\partial \hat{\lambda}_N}{\partial \alpha_1} & \frac{\partial \hat{\lambda}_N}{\partial \alpha_2} & \cdots & \frac{\partial \hat{\lambda}_N}{\partial \alpha_n} \end{bmatrix} \quad (7)$$

In equation (7) N is the number of extension ratios and n is the number of parameters. The matrix S was calculated at each iteration of the feedback loop in the block-diagram in Fig. 3. A finite difference method was used to calculate the column vectors in S: First, the simulation result using the parameters $\underline{\alpha}_k$ was entered in the column vector $\hat{\underline{\Lambda}}_0$. Then, parameter m in $\underline{\alpha}_k$ was increased by 10% while the other parameters were kept the same as in the original $\underline{\alpha}_k$. The FE simulation was run and the result written into column vector $\hat{\underline{\Lambda}}_m$. Column m of S was calculated as $(\hat{\underline{\Lambda}}_m - \hat{\underline{\Lambda}}_0) / \Delta \alpha_m$. When all the columns in S were calculated, the parameter increment \underline{h} was found as shown in equation (6). The new parameters were found using $\underline{\alpha}_{k+1} = \underline{\alpha}_k + \underline{h}$. If the components of the incremental vector \underline{h} were below certain thresholds the iteration process was stopped as the parameters were considered to have converged.

2.5 Sensitivity Analysis

An analysis of the method's ability to estimate the parameters was performed. The matrix S expresses the model response sensitivity to variations of the material parameters. If the variation of one parameter causes a similar response as the variation of another, the estimation process might be ambiguous. This will result in two almost dependent column vectors in S for the corresponding parameters. To analyze the correlation between the various parameters' influence on the model-response each column in S was normalized creating the matrix s and hence the sensitivity matrix s^T s, in which a value close to ± 1 for element e_{ij} means the parameter i and j are highly correlated. A high correlation may result in a non-converging estimation problem. A solution is then to put one of two correlated parameters to a constant value and estimate only one of them.

If a variation of one parameter makes little difference on the model response, it will be difficult to estimate this parameter and the parameter's influence on the deformation may be minor. We compared the sensitivity of the model response to a variation in each parameter by looking at the norm of the column vector $(\hat{\Lambda}_m - \hat{\Lambda}_0)$.

It was considered unlikely that the estimation procedure could estimate all 9 parameters unambiguously. The above analysis helped us rule out several parameters and left us with three parameters to estimate – one in each of the axial directions. These three parameters were used in the further analysis of the method.

Several tests were performed to check the convergence of the estimates of the three parameters (the other parameters were set to constant values). First the three parameters were estimated while the others were set to their correct (known) values. Then, the estimation was carried out while the other parameters were set to incorrect values, making the material either stiffer or softer than the true material. To make the material stiffer the constant k 's and b 's were increased with 20% while the poles were decreased by 20%. To make it softer the opposite changes were made. Note that the value of the denominator is most often below 1 in the terms of equation (1). Thus, an increase of the exponential b will increase the energy of the term and make it stiffer. Fig. 4a shows stress-strain curves in the fiber direction with different parameter sets. The solid curve is calculated with the true parameter values ($k_1=2.0$, $a_1=0.523$, $b_1=1.351$). The dashed curve is the initial stiffer guess where the parameters are changed by 20% ($k_1=2.4$, $a_1=0.4184$, $b_1=1.6212$).

The next test was to add noise to the test data, $\lambda_i + w_i$, and check the convergence of the estimated parameters. The convergence was examined for different levels of noise w_i (w_i = random numbers uniformly distributed in the intervals): $w_i = 0$ (no noise), $w_i \in [-0.01, 0.01]$, $w_i \in [-0.05, 0.05]$, and $w_i \in [-0.1, 0.1]$.

The last test was both to add noise to the test data and to set the other parameters to constant incorrect values and then run the estimation procedure.

3 Results

The analysis of the sensitivity matrices resulting from the estimation of all 9 parameters showed a high correlation between several of the parameters. There was an obvious pattern to the correlation. The three parameters k_1 , a_1 , and b_1 were highly correlated with each other. So were k_2 , a_2 , and b_2 . Table 2 shows an average of two sensitivity matrices: one where the parameter increment was +10% to calculate the S matrix, and one where the increment was -10%. The model response had substantially higher sensitivity to variations of the parameters in the fiber and sheet directions than in the sheet-normal direction (Table 3). The highest sensitivities within the three directions were for changes of the pole parameters (a_1 , a_2 , and a_3).

	k_1	a_1	b_1	k_2	a_2	b_2	k_3	a_3	b_3
k_1	1.00	-0.99	0.99	0.77	-0.87	0.78	0.32	-0.50	0.34
a_1	-0.99	1.00	-0.99	-0.75	0.86	-0.75	-0.32	0.53	-0.37
b_1	0.99	-0.99	1.00	0.77	-0.86	0.77	0.31	-0.50	0.33
k_2	0.77	-0.75	0.77	1.00	-0.93	0.99	0.43	-0.19	0.49
a_2	-0.87	0.86	-0.86	-0.93	1.00	-0.93	-0.55	0.53	-0.39
b_2	0.78	-0.75	0.77	0.99	-0.93	1.00	0.43	-0.19	0.49
k_3	0.32	-0.32	0.31	0.43	-0.55	0.43	1.00	-0.59	0.27
a_3	-0.50	0.53	-0.50	-0.19	0.53	-0.19	-0.59	1.00	0.01
b_3	0.34	-0.37	0.33	0.49	-0.39	0.49	0.27	0.01	1.00

Table 2. Sensitivity matrix. Average result of two sensitivity matrices: one where the parameter increment was +10% and one with a -10% increment. The values are a reflection of the correlation between two parameters, i.e. a value close to 1, means a change in one parameter has a similar effect on the model output to a change of the other parameter.

k_1	a_1	b_1	k_2	a_2	b_2	k_3	a_3	b_3
0.04406	0.07057	0.04785	0.04224	0.06361	0.02185	0.00918	0.01293	0.00013

Table 3. Sensitivity values. Average of two sensitivity values for each parameter: one where the parameter increment was +10% and one with a -10% increment. Each value is calculated as the norm of the vector that contains the difference at each measurement point between the model response with one perturbed parameter ($\pm 10\%$) and the model response simulated with the true parameter values.

From the results of the sensitivity analysis it was decided to estimate only one parameter in each direction. It was observed that a change of either the pole 'a' or the curvature parameter 'b' could compensate better for wrong values in the two other parameters than the coefficient parameter 'k' (see Fig. 4a). From these results we chose to estimate the poles a_1 , a_2 , and a_3 .

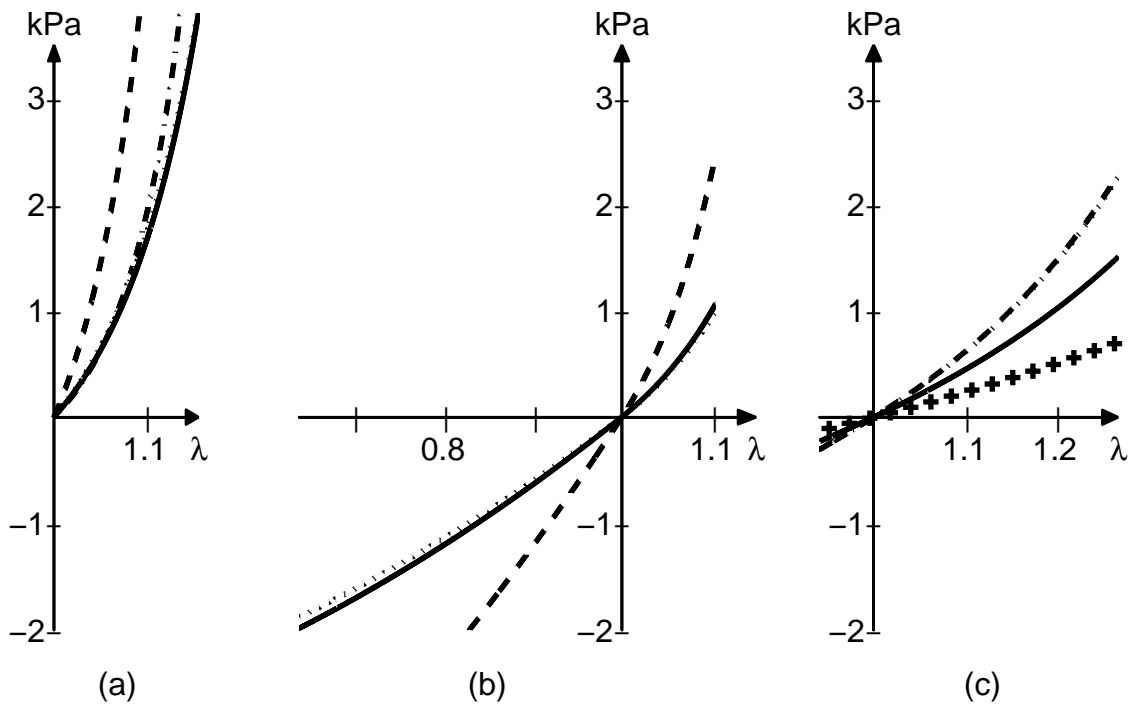


Figure 4. Stress-stretch relationship in fiber (a), sheet (b), and sheet-normal (c) directions. The solid lines are the relationships using the true parameter values in Table 1. The dashed lines are the relationships when each of the parameters is changed to a 20% stiffer value. The dotted lines are the result after the estimation procedure ($a_1=0.63$, $a_2=0.84$, $a_3=0.83$). The dash-dotted line in (a) is when $k_1 (=1.06)$ is estimated instead of a_1 . The + line in (c) is the result of $a_3=3.29$ in the case when the constant parameters are set 20% softer. Note that the dotted line in (a) almost overlaps the solid line, while in (c) the dotted line almost overlaps the dashed line. The abscissas are the ranges of fiber, sheet, and sheet-normal stretches. The minimum and maximum stretch range for each of the three plots is obtained by finding the minimum and maximum stretch of all the LV Gauss points in each respective direction of the simulation result.

The first trial was to estimate the three chosen parameters with the other constant parameters set to their true values. Initially, the estimated parameters were set $\pm 20\%$ off their true values. With no added noise a_1 and a_2 had practically converged to their true values after a single iteration. The same was the case for a_3 after two iterations. Table 4 summarizes the estimation results after three iterations. Fig. 5a-c shows the convergence of the parameter a_1 , a_2 , and a_3 , respectively. Initial values of $\pm 50\%$ and $\pm 75\%$ off their true values were tested. A change of 50% of the pole value gives a substantial shift of its stress-strain curve. All 8 combinations of setting: a_1 , a_2 , and a_3 too low; a_1 , a_2 too low and a_3 too high; etc; to the last combination of a_1 , a_2 , and a_3 too high, were also tested. These tests converged as well, but needed 1-4 more iterations in some cases.

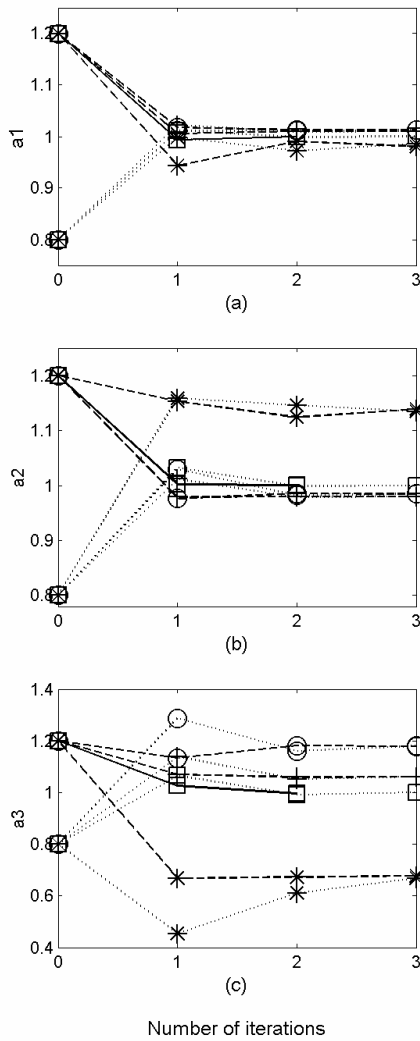


Figure 5. Convergence of parameters a_1 , a_2 , and a_3 in (a), (b), and (c), respectively. The plots are normalized with respect to their true parameter values. The convergence of the parameters with different levels of noise added to the measurements is shown with different line-markers; \square : $w_i = 0$ (no noise), $+$: $w_i \in [-0.01, 0.01]$, O : $w_i \in [-0.05, 0.05]$, and $*$: $w_i \in [-0.1, 0.1]$. The initial values were offset by +20% (dashed lines) and -20% (dotted lines) from their true parameter values.

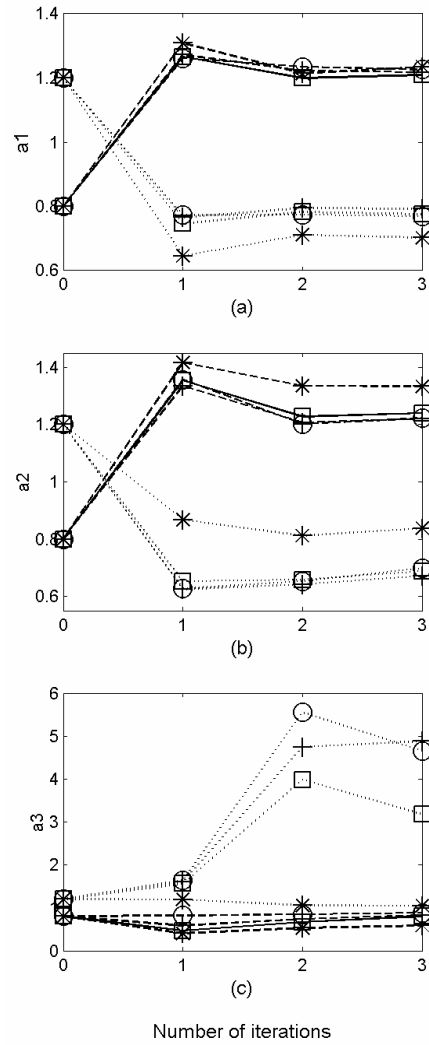


Figure 6. Convergence of parameters a_1 , a_2 , and a_3 in (a), (b), and (c), respectively, when the values of the constant parameters, the k 's and b 's, are set 20% too high/stiff (dashed lines) and -20% too low/soft (dotted lines). The plots are normalized with respect to their true parameter values. The convergence of the parameters with different levels of noise added to the measurements is shown with different line-markers; \square : $w_i = 0$ (no noise), $+$: $w_i \in [-0.01, 0.01]$, O : $w_i \in [-0.05, 0.05]$, and $*$: $w_i \in [-0.1, 0.1]$. Initially, the start values of the poles are decreased 20% to make the material even stiffer (dashed lines) or increased 20% to make it even softer (dotted lines).

noise	Correct k's and b's				Too stiff k's and b's $1.2 \times k_{i_true}, 1.2 \times b_{i_true}$				Too soft k's and b's $0.8 \times k_{i_true}, 0.8 \times b_{i_true}$			
	0	[±0.01]	[±0.05]	[±0.10]	0	[±0.01]	[±0.05]	[±0.10]	0	[±0.01]	[±0.05]	[±0.10]
a ₁	0.52	0.53	0.53	0.52	0.63	0.64	0.64	0.65	0.41	0.41	0.40	0.37
a ₂	0.68	0.67	0.67	0.77	0.84	0.83	0.83	0.91	0.47	0.46	0.48	0.57
a ₃	1.04	1.10	1.22	0.70	0.83	0.86	0.92	0.61*	3.29	5.06	4.82	1.09

Table 4. Estimation results. The values after three iterations of the estimated poles a_1 , a_2 , and a_3 with different ranges of noise and different values of the constant k and b parameters. For the value marked with *, see text.

As shown in Fig. 5 the fiber pole, a_1 , converged quickly and with just a small offset ($< \pm 2.5\%$ off) from its true value for all three levels of noise added to the test data. The sheet pole parameters, a_2 , converged quickly and with small offset ($< \pm 2.5\%$ off) from its true value for the two lowest levels of noise, for the highest noise level it ended up on a value 13% higher than its true value. The sheet-normal pole, a_3 , ended up with offsets of 6%, 18%, and -33% for the three levels of noise added, respectively.

Fig. 6 shows the convergence of the parameters when all the parameters were changed 20% in the stiffer direction (dashed lines) and 20% in the softer direction (dotted lines). The estimation results are summarized in Table 4. In general the estimated values of a_1 and a_2 converged to values that compensated for the incorrect constant parameter values of the k 's and b 's as can be seen in the case of initial too stiff parameters in Fig. 4. The sheet-normal pole, a_3 , converged to a paradoxical value, i.e. it got even more stiff or soft when k_3 and b_3 were set too stiff or soft, respectively. The convergence pattern for a_3 was also quite oscillatory. In the case of too stiff k_3 and b_3 and the highest noise level, the value of a_3 was -0.35 after the first iteration. An automatic correction routine in the estimation code changed the unphysiological value and replaced it with half its previous value (0.4148) as shown in Fig. 6. From then on the parameter converged.

The computation time needed for the estimation depended on the number of estimated parameters. One forward FE simulation required approximately 80 seconds using 15 CPUs on an Origin 3800L SGI machine with 600 MHz R14k processors. For every iteration in the estimation routine, one FE simulation was done for each estimated parameter plus one with the updated parameter set, i.e. four FE simulations for every iteration when three parameters were estimated.

4 Discussion

The finite element method is a powerful tool to calculate strain and stress distributions in loaded structures with a complex geometry, but for accurate stress calculations the material properties need to be known. In this study we have presented a model-based estimation procedure where we have applied the FE method to characterize the stress-

strain relationship in passive LV myocardium. We have used a 3D FE model of the LV myocardium that includes finite deformation theory, morphological fiber and sheet structure, and a non-linear orthotropic constitutive law. The estimation procedure is based on measured strains (from for example tagged MRI) where the measured strains are compared with the model-predicted strains and the errors between the two are minimized in a least-squares sense by optimizing the material parameters in the model.

The investigation of the parameter observability showed a high degree of coupling between some of the parameters. The three parameters in the fiber direction were highly correlated; so were the three parameters in the sheet direction as seen in Table 2. The correlation may be explained by the similar response of the stress-strain curve when the parameters are varied. An increase in k and b both raise the curve and vice versa. An increase of the pole parameter, a , lowers the stiffness curve and vice versa. Thus, parameters k and b are positively correlated, while they are negatively correlated with parameter a as seen in Table 2. The close relationship between the parameters is shown in Fig. 4. Fig. 4a shows the true fiber stiffness curve (solid line), a curve where k_1 and b_1 are increased by 20% and a_1 is decreased by 20% to make it stiffer (dashed line). The dotted curve (practically overlapping the solid line) has the same parameters as the stiffer one except a_1 , which has been estimated using the parameter estimation method. The estimation resulted in a 20% higher value of a_1 compared to its true value. This increase of a_1 compensates for the increased stiffness in k_1 and b_1 and the resulting stress-strain relationship is almost identical to the true curve. The dash-dotted line shows the similar, but in this case parameter k_1 is estimated instead of a_1 . The reduction of k_1 compensates for the increased stiffness in b_1 and a_1 . The compensation with the pole parameter a_1 gives a better fit to the true curve than with the scaling parameter k_1 . Outside the range of strain plotted in the figure the curves will diverge but we believe the strains are limited to approximately this range in the phase between the beginning of diastasis and the end of diastole. An important point here is that the pole-zero terms in the strain energy function (1) are designed to represent the full range of elastic strain but the parameters are in fact only being fitted for a limited portion of this range. This means that the curve is over parameterized for these tests and that what is significant is the fitted stress-strain curve, not the individual parameter values. Future tests over wider ranges of strain are needed to better characterize the individual parameter values.

The high degree of coupling between the parameters may make it difficult to estimate all of them and get proper convergence. But from the results showing the compensation of wrong values on two parameters by a change of the third parameter value, we believe it may be possible to estimate the stress-strain characteristics by estimating only one parameter in each direction. The choice falls on the estimation of the pole parameters a_1 , a_2 , and a_3 which yield closer fits to the stress-strain curves and give the highest model response sensitivities in their respective directions. The estimation of a_1 and a_2 showed good robustness. They converged well for all cases with added noise and wrong values of the other parameters. There was more uncertainty connected to the estimation result of the sheet-normal pole a_3 . With correct values of the k and b parameters, a_3 was estimated with a fair degree of accuracy. The error of the estimate was dependent on the degree of noise in the test data. However, when the constant parameters were set too

stiff, a_3 ended up with a value that made the sheet-normal characteristic even stiffer and vice versa.

There may be different reasons for the poorer estimate of a_3 . The contribution to the total strain energy from the sheet-normal term in equation (1) is the lowest of the axial terms as can be seen in Fig. 2 and 4. Thus the sensitivity of the model output to a variation in a sheet-normal parameter would be lower than for a parameter in the fiber or sheet direction, which is seen in Table 2. It may then be that the fiber and sheet stiffness cause the limiting deformation and a variation of the sheet-normal stiffness is so soft it makes little difference. In this study we have not attempted to estimate any shear parameters. Dokos et al. [3] conclude that the contribution of shear stiffness to the passive LV deformation is relatively small, so the sensitivity to a change in a shear parameter is likely to be small.

During diastole the LV is elongated and the wall thins. The fibers are stretched, the myocardial sheets lie primarily in the transmural direction and are mostly compressed, whereas there is mainly a stretch in the sheet-normal direction which is primarily aligned with the base-apex direction. During systole the opposite occurs. Since the sheet-pole governs the limiting stretch of the sheet it may seem more appropriate to estimate this parameter during systole while the sheets are mostly stretched.

In this study we wanted to investigate the feasibility of the estimation procedure and we generated a set of test data from simulations instead of using real strain measurements. This enabled us to evaluate the results against the known solution and to analyze the effects of noise and model error. The results encourage the validation of the method on real measurement data. In a clinical study measured strains from for example tagged magnetic resonance images would replace the generated test data. When the method is used on real measurements some errors may arise that are not apparent in this study.

The boundary conditions on the FE model may be a source of error. The effects of the pericardium, the intersections with the right ventricle (RV), and the RV pressure on the septum are all ignored in the boundary conditions.

Another factor that may influence the results is that the LV is not necessarily in an unloaded state, i.e. the LV pressure $\neq 0$ mmHg, at the beginning of diastasis. This pressure will produce stresses and strains that arise in addition to the residual strains and stresses in the unloaded reference state. A better approximation to the initially reference configuration of our FE model may be to first inflate the model from 0 mmHg to the measured pressure at the beginning of diastasis. Then import the calculated nodal stresses and strains back to the initial geometry and use this as the starting configuration of the estimation routine. This approximation assumes that the strains caused by the non-zero pressure are small and that the stress-strain relationship for these small strains is approximately linear.

We have assumed that the fiber and sheet orientations are the same in all hearts and have not looked into the effects of possible variations of the fiber and sheet orientations in different hearts. In regionally diseased hearts such as in the case of ischemia and

infarction there are likely to be regional variations of the stiffness of the myocardium. This may even be the case in normal hearts [17]. We have assumed a homogenous set of material parameters throughout the LV myocardium. A further development of the method may include regionally varying material parameters. Extension of the method to include regions with different material parameters may be done by adding a set of parameters per region to the estimation routine. However, there is likely to be a limit to the number of observable parameters.

Acknowledgement

This research has been supported in part by The Research Council of Norway grants # 128267/320 and #139327/300 and through a grant of computing time (Program for supercomputing).

References

- [1] P. M. F. Nielsen, P. J. Hunter, B. H. Smaill, "Biaxial testing of membrane biomaterials: Testing equipment and procedures," *J. Biomech. Eng.*, vol. 113, pp. 295-300, Aug. 1991.
- [2] S. Dokos, I. J. LeGrice, B. H. Smaill, J. Kar, A. A. Young, "A triaxial-measurement shear-test device for soft biological tissues," *J. Biomech. Eng.*, vol. 122, pp. 471-478, Oct. 2000.
- [3] S. Dokos, B. H. Smaill, A. A. Young, I. J. LeGrice, "Shear properties of passive ventricular myocardium," *Am. J. Physiol.*, vol. 283, pp. H2650-H2659, Dec. 2002.
- [4] M. J. Moulton, L. L. Creswell, R. L. Actis, K. W. Myers, M. K. Vannier, B. A. Szabo, M. K. Pasque, "An inverse approach to determining myocardial material properties," *J. Biomech.*, vol. 28, pp. 935-948, Aug. 1995.
- [5] M. J. Moulton, L. L. Creswell, S. W. Downing, R. L. Actis, B. A. Szabo, M. K. Pasque, "Myocardial material property determination in the in vivo heart using magnetic resonance imaging," *Int. J. Card. Imaging*, vol. 12, pp. 153-167, Sep. 1996.
- [6] I. J. LeGrice, P. J. Hunter, B. H. Smaill, "Laminar structure of the heart: a mathematical model," *Am. J. Physiol.*, vol. 272, pp. H2466-H2476, May 1997.
- [7] B. H. Smaill, P. J. Hunter, "Structure and function of the diastolic heart: Material properties of passive myocardium," in: *Theory of heart: biomechanics, biophysics, and nonlinear dynamics of cardiac function*, L. Glass, P. J. Hunter, A. D. McGulloch, Eds., New York: Springer-Verlag, 1991, pp. 1-29.
- [8] P. J. Hunter, "Myocardial constitutive laws for continuum mechanics models of the heart," *Adv. Exp. Med. Biol.*, vol. 382, pp. 303-318, 1995.
- [9] M. P. Nash, P. J. Hunter, "Computational mechanics of the heart: from tissue structure to ventricular function," *J. Elasticity*, vol. 61, pp. 113-141, 2000.

- [10] C. Stevens, E. Remme, I. LeGrice, P. Hunter, "Ventricular Mechanics in diastole: material parameter sensitivity". *J. Biomech.*, vol. 36, pp. 737-748, May 2003.
- [11] K. D. Costa, P. J. Hunter, J. S. Wayne, L. K. Waldman, J. M. Guccione, A. D. McCulloch, "A three-dimensional finite element method for large elastic deformations of ventricular myocardium: Part II – Prolate spherical coordinates," *J. Biomech. Eng.*, vol 118, pp. 464-472, Nov. 1996.
- [12] P. J. Hunter, P. M. Nielsen, B. H. Smaill, I. J. LeGrice, I. W. Hunter, "An anatomical heart model with applications to myocardial activation and ventricular mechanics," *Crit. Rev. Biomed. Eng.*, vol. 20, pp. 403-426, 1992.
- [13] I. LeGrice, P. Hunter, A. Young, B. Smaill, "The architecture of the heart: a data-based model," *Philos. Transact. Ser. A Math. Phys. Eng. Sci.*, vol. 359, pp. 1217-1232, Jun. 2001.
- [14] J. H. Omens, Y. C. Fung, "Residual strain in the rat left ventricle," *Circulation Research*. Vol. 66, pp. 37-45, 1990.
- [15] E. K. Rodriguez, A. Hoger, A. D. McCulloch, "Stress-dependent finite growth in soft elastic tissue," *J. Biomech.*, vol. 27, pp. 455-467, 1994.
- [16] K. D. Costa, K. May-Newman, D. Farr, W. G. O'Dell, A. D. McCulloch, J. H. Omens, 1997. "Three-dimensional residual strain in midanterior canine left ventricle," *Am. J. Physiol.*, vol. 273, pp. H1968- H1976, 1997
- [17] V. P. Novak, F. C. Yin, J. D. Humphrey, "Regional mechanical properties of passive myocardium," *J. Biomech.*, vol. 27, pp. 403-412, 1994.

Paper C

Parameter distribution models for estimation of left ventricular deformation using sparse fiducial markers.

Espen W. Remme^{1,2}, Kevin F. Augenstein², Alistair A. Young^{2,3}, Peter J. Hunter²

¹Department of Circulation and Medical Imaging, NTNU, Trondheim, Norway

²Bioengineering Institute, University of Auckland, New Zealand

³Department of Anatomy with Radiology, University of Auckland, New Zealand

Accepted in IEEE Transactions on Medical Imaging with new title:

Parameter distribution models for estimation of population based left ventricular deformation using sparse fiducial markers

Paper D

Extraction and quantification of left ventricular deformation modes.

Espen W. Remme^{1,2}, Alistair A. Young^{2,3}, Kevin F. Augenstein², Brett Cowan⁴,
Peter J. Hunter²

¹Department of Circulation and Imaging, NTNU, Trondheim, Norway

²Bioengineering Institute, University of Auckland, New Zealand

³Department of Anatomy with Radiology, University of Auckland, New Zealand

⁴Department of Medicine, University of Auckland, New Zealand

In press in IEEE Transactions on Biomedical Engineering

Paper E

The influence of material properties on left ventricular deformation in an elliptical model

Espen W. Remme^{1,2} and Peter J. Hunter²

¹Department of Circulation and Imaging, Norwegian NTNU, Trondheim, Norway

²Bioengineering Institute, University of Auckland, New Zealand

Abstract

In this study we have investigated the effect of variations of the material properties on left ventricular (LV) deformation in a simulation model. An elliptically shaped finite element (FE) model was used as an approximation to the LV wall geometry. The model incorporated a description of the varying myocardial fiber and sheet orientations through the wall together with a passive orthotropic constitutive law and a steady state active law that generated a stress component along the fibers during systole. The inflation phase, isovolumetric contraction phase, and ejection phase were simulated by applying appropriate boundary conditions on the model through the various phases. The deformation of the FE mesh that occurred between the end diastolic mesh configuration (after the inflation phase) and the end systolic mesh (end ejection) was decomposed into different deformation modes such as wall thickening and longitudinal shortening using a previously developed method. To investigate the effects of the material parameter values on the deformation modes, we repeated the simulation with varying material parameters. The result showed reduced wall thickening with stiffer passive properties along the fiber direction. Stiffer sheets resulted in a pronounced reduction of both wall thickening and longitudinal shortening. Changes of the sheet-normal stiffness had little effect on the modes except for moderately reduced longitudinal shortening for stiffer parameter values. Increased sheet - sheet-normal shear stiffness reduced wall thickening. The majority of the results were consistent with other studies and the variations in deformation modes could for the most part be interpreted in terms of myocardial microstructure and orientation.

Unpublished

1 Introduction

The material properties of the myocardium have a major impact on the deformation of the heart wall during the cardiac cycle. A change of these properties caused by myocardial disease results in an altered deformation pattern. A most dramatic example is the effect of myocardial scar tissues that occur after myocardial infarction and impairs ventricular pump function [1]. Also diffuse heart disease may alter myocardial structure and function. Patients with diabetes mellitus are for example more likely to show signs of abnormal relaxation of the myocardium and elevated left ventricular (LV) filling pressure. Histologically, these patients have interstitial fibrosis with increased amounts of collagen, glycoprotein, triglycerides, and cholesterol in the myocardial interstitium [2].

We have previously found that the LV deformation pattern between end diastole (ED) and end systole (ES) of a group of patients with diabetes mellitus differs significantly from that of a group of normal subjects [3]. For that purpose a finite element mesh was used to describe the geometry of the LV. The LV deformation was calculated by fitting the motion of the mesh to measured magnetic resonance tissue tagged data from each subject. The deformation of the FE mesh was decomposed and quantified into several deformation modes such as longitudinal shortening, wall-thickening, and longitudinal twist and the magnitude of each mode was compared between the patients and the normal subjects. We speculated that the observed difference in the deformation pattern between the two groups was partly due to differences in the underlying myocardial structure. Studies of the microstructure of the myocardial tissue have revealed that the myocardial fibers are organized in lamina or sheets about four cells thick and that the cells are tightly coupled by collagen within the sheets while the sheets are only loosely bound together. This orthotropic architecture has three distinct axes: one along the myocyte or 'fiber direction', one normal to the fiber but in the sheet, and one normal to the sheet [4]. Recent investigations have shown that the microstructural arrangement of the myocardial tissue and the varying orientation of the material axes through the heart wall have significant impact on the total wall deformation. LeGrice et al. [5] showed that a major contribution to wall thickening that occurs during systole is the shearing of myocardial sheets in the subendocardium. Costa et al. [6] showed that stretching of the sheets and shear between the sheets contributes to the majority of the wall thickening.

FE models of the ventricular walls have been developed during the last decades and evolved to include a description of the varying material microstructure as well as an orthotropic constitutive law capable of solving the large deformation problems that occur during the heart cycle [7]. To gain a better understanding of the influence of material properties on the deformation we studied the effects of varying the myocardial stiffness in the different material directions in an FE simulation model of the LV. The aim of this study was thus to construct an LV FE model and simulate the deformation of the model that occurred from the beginning of diastasis to end ejection with varying material parameters in the model. The deformation is decomposed into different deformation modes and the effect of the parameter variations on each deformation mode is quantified.

2 Methods

A detailed description of an FE model for solving cardiac mechanics similar to the one used in this study can be found in [7]. A brief description of the model follows below.

2.1 Finite Element Model - Geometry

An FE mesh with the shape of a truncated ellipsoid was used to approximate the LV geometry as shown in Fig. 1. The mesh had four elements circumferentially and longitudinally, and three elements transmurally giving a total of 48 elements and 68 nodes. A rectangular Cartesian coordinate system was used with tricubic Hermite interpolation for the geometry. The elements were aligned so that the element coordinate ξ_1 was in the circumferential direction, ξ_2 in the longitudinal direction, and ξ_3 in the transmural direction, see Fig. 1. The fiber and sheet angles were set to vary linearly through the wall with a fiber angle of 85° and a sheet angle of -45° at the endocardial nodes and -75° and 45° , respectively, at the epicardial nodes [4], [8]. The fiber angle is given with respect to the circumferential direction in the ξ_1 - ξ_2 plane, while the sheet angle is given with respect to the radial ξ_3 -coordinate (orthogonal to the fiber angle) where sheet angles above the radial direction are recorded as positive.

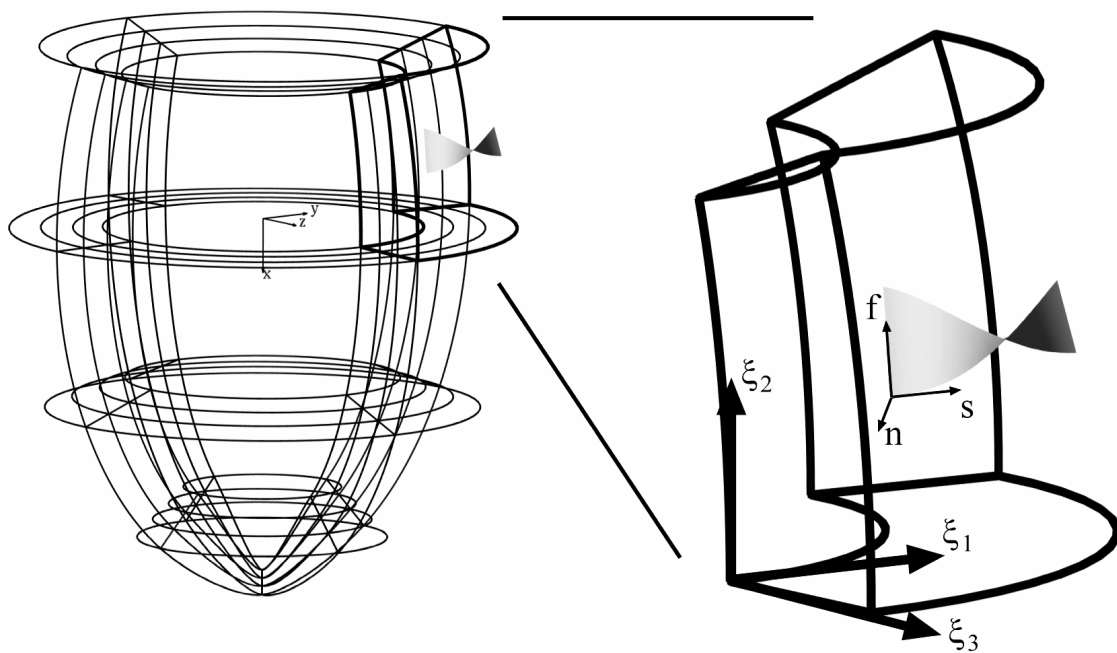


Figure 1. The FE mesh of the truncated ellipsoid used as an approximation to the LV geometry. The mesh consists of four circumferential, four longitudinal, and three transmural elements. An enlargement of an element that extends over the whole transmural direction from the endocardial to epicardial surface (marked with bold lines on the left) is shown on the right. The rectangular Cartesian coordinate system is shown for the mesh on the left while the element (ξ_i) coordinates are shown for the element on the right together with a myocardial fiber-sheet illustrating the varying angles of the fibers and sheet through the heart wall: f - fiber direction, s - sheet direction, and n - sheet-normal direction.

2.2 Passive Constitutive Law

The passive material properties were modeled using the orthotropic ‘‘pole-zero’’ strain energy function (1) proposed in [9]. In equation (1) index 1 refers to the fiber direction, index 2 refers to the sheet direction, and index 3 refers to the sheet-normal direction. e_{ij} are the covariant components of Green’s strain tensor referred to these axes. (Note that these are physical components of strain because they are referred at each point to normalized orthogonal rectangular Cartesian coordinates.) There are three different types of parameter in the constitutive equation: a_i are the poles or the limiting strains, b_i are related to the curvature of the uniaxial stress-strain relationships, and k_i are the relative weights of each term to the total strain energy. The components of the 2nd Piola-Kirchhoff stress tensor are derived from the strain energy function in equation (2) for the strain components in the fiber-sheet material coordinate system (v_α). The material is assumed to be incompressible so a hydrostatic pressure term is added where p is the hydrostatic pressure and $a_{(v)}^{\alpha\beta}$ is the contravariant metric tensor for the v_α -coordinate system in the deformed configuration. For the three axial directions the pole-zero law was used only for positive strain (stretch). For compressive strain a linear stress-strain relationship was used in the three axial directions where the slope was the derivative of (1) with respect to the respective direction at zero strain. The stress-strain relationships for negative shear strains were set to be the same as the relationships for positive shear strains but with opposite sign, i.e. mirrored about the origin.

$$W = k_1 \frac{e_{11}^2}{(a_1 - e_{11})^{b_1}} + k_2 \frac{e_{22}^2}{(a_2 - e_{22})^{b_2}} + k_3 \frac{e_{33}^2}{(a_3 - e_{33})^{b_3}} + k_4 \frac{e_{12}^2}{(a_4 - e_{12})^{b_4}} + k_5 \frac{e_{13}^2}{(a_5 - e_{13})^{b_5}} + k_6 \frac{e_{23}^2}{(a_6 - e_{23})^{b_6}} \quad (1)$$

$$T^{\alpha\beta} = \frac{1}{2} \left(\frac{\partial W}{\partial e_{\alpha\beta}} + \frac{\partial W}{\partial e_{\beta\alpha}} \right) - p a_{(v)}^{\alpha\beta} \quad (2)$$

2.3 Active Law

During systole an active stress component, T_0 , was added along the fiber direction. The active component was calculated using a simple steady state equation [10] shown in (3). The first factor of (3) is a sigmoidal Hill function going from 0 to approximately 1 as the activation parameter, Ca_{actn} , is changed from 0 to 1. The second part is a linear stress relationship as a function of fiber stretch λ .

$$T_0(\lambda, Ca_{actn}) = \frac{(Ca_{actn} \cdot [Ca^{2+}]_{\max})^h}{(Ca_{actn} \cdot [Ca^{2+}]_{\max})^h + (c_{50})^h} \cdot T_{ref} (1 + \beta(\lambda - 1)) \quad (3)$$

2.4 Residual Strains

Residual strains [11] in the fiber direction were included in the reference configuration using the method of Rodriguez et al. [12]. The residual fiber strains varied linearly with a 5% stretch at the epicardium and a 5% contraction at the endocardium [13].

2.5 Boundary Conditions

In a real heart the LV motion is influenced by the RV, the atria and the pericardium. Our LV mesh was isolated so certain constraints were imposed to the mesh to restrict the motion. The long axis of the LV was aligned with the x-axis. The x-coordinate and its derivatives $\partial x/\partial \xi_1$, $\partial x/\partial \xi_3$, and $\partial^2 x/(\partial \xi_3 \partial \xi_1)$ were fixed for the base nodes during the simulations. All the apical nodes were fixed to lie on the x-axis but free to move in the x-direction, allowing for thickness change of the apex and a general longitudinal base-apex length change. The two endocardial base nodes on the z-axis had their y-coordinate fixed, while the z-coordinate was fixed for the two endocardial nodes on the y-axis. This prevented any rigid body rotation of the mesh.

2.6 Simulation of the Inflation Phase

The various phases of the cardiac cycle are illustrated in a Wiggers diagram in Fig. 2. The simulation of the cardiac cycle was started from the beginning of diastasis (VII in Fig. 2) as it was assumed that the myocardium at that stage was at its most stress-free state. During the diastasis and atrial contraction phase (VII – IX in Fig. 2) the LV is being passively inflated, i.e. the LV myocardium is in a passive state with no active generated fiber stress. This was simulated by setting the Ca_{actn} parameter in (3) to zero and incrementing the pressure from 0 to 0.5 kPa on the surfaces of the elements that made up the endocardial wall. The resulting deformed mesh was saved as the ED mesh.

2.7 Simulation of the Isovolumetric Contraction Phase

The electrical activation of the myocardium propagates rapidly through the whole ventricular wall after it has passed the atrioventricular node. The myocardial fibers start to actively contract, increasing the LV pressure beyond the left atrial pressure and thus closing the mitral valve. As the fibers keep contracting the LV pressure keeps increasing. The pressure in the ascending aorta is approximately 10 kPa and the aortic valve stays closed until the LV pressure exceeds the aortic pressure. Thus, during the phase between mitral valve closure and aortic valve opening the LV cavity volume is constant (I – II in Fig. 2). To simulate this isovolumic contraction (IVC) phase a set of incompressible cavity elements was included in our model. The cavity elements were coupled with the wall elements through shared endocardial nodes and face pressure constraints. Active contraction was simulated by gradually increasing Ca_{actn} equally at all parts throughout the ventricular wall. This increased the tension along the fiber direction, which caused the wall elements to deform around the cavity region, also moving the coupled endocardial nodes. The displacement of the endocardial nodes deformed the cavity elements, which were restricted to maintain a constant volume and this constraint gave rise to a hydrostatic pressure for the cavity region. This hydrostatic pressure was equivalent to the cavity pressure and it was coupled with the wall elements

by applying the pressure as a boundary constraint at the endocardial surface of the wall elements. The activation parameter was increased until the cavity pressure reached 10 kPa marking the opening of the aortic valve and the end of the IVC.

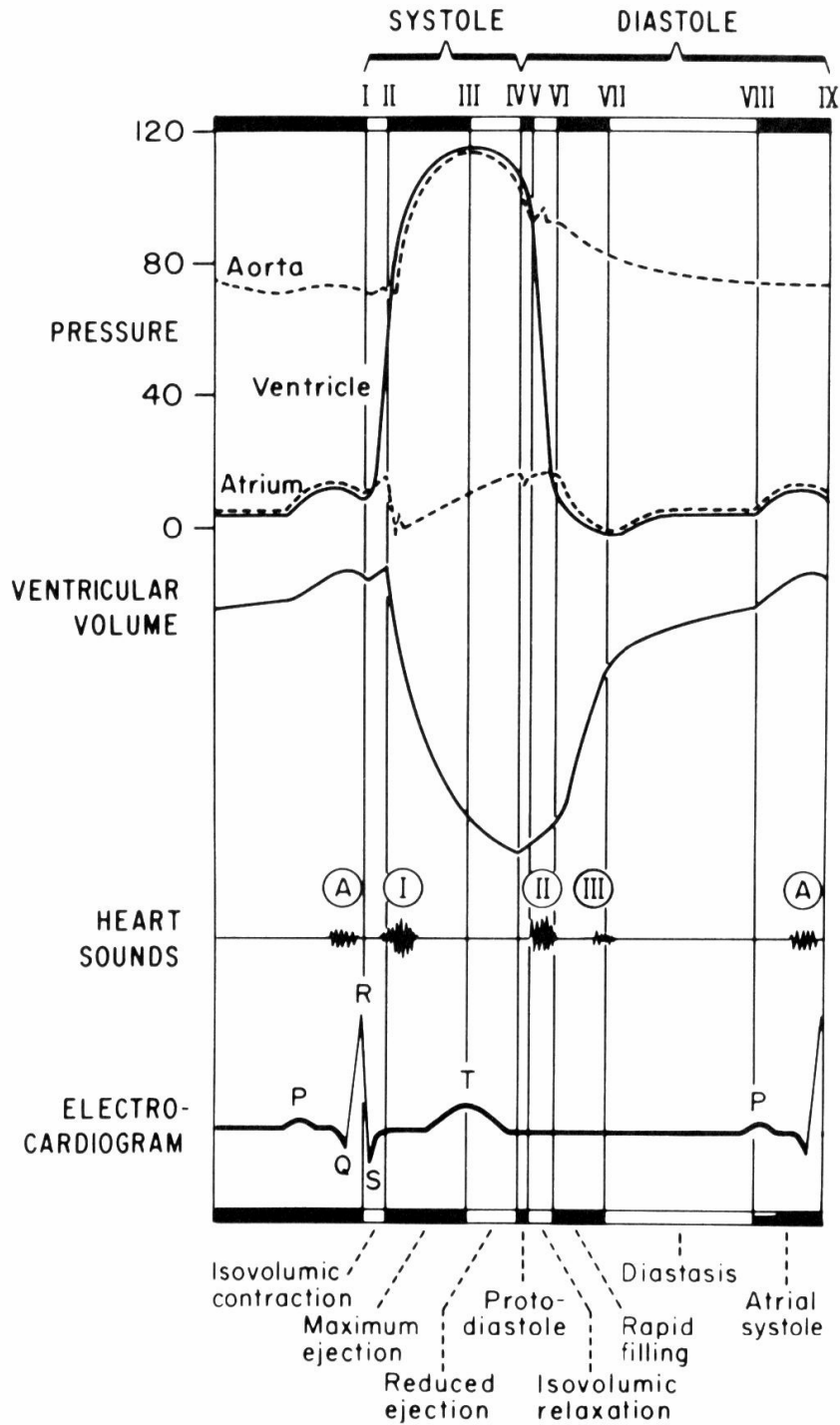


Figure 2. A Wiggers diagram illustrating the phases of the cardiac cycle. Note that the pressure values in the figure are given in mmHg while typical pressure values are given in kPa in text. Reproduced from [14(a)].

2.8 Simulation of the Ejection Phase

When the aortic valve opens the blood is pumped from the ventricle into the aorta as the fibers keep contracting (II – IV in Fig. 2). Normally about 55 – 75% of the blood in the LV cavity is pumped out during the ejection phase [14(b)]. The pressure increases to a maximum of approximately 15 kPa then decreases to about 14 kPa during the reduced ejection phase just before the aortic valve closes at end ejection (III – IV in Fig. 2). After the IVC phase the activation parameter was usually about 0.38. During the simulation of the ejection phase this value and the applied pressure on the endocardial surface of the wall elements were increased incrementally to reach 1.0 and 15 kPa, respectively. As a result of the increased fiber tension, the fibers contracted resulting in a general wall thickening, longitudinal shortening and reduced cavity volume. (The cavity elements were no longer included for the simulation of the ejection phase.) The reduced ejection phase was simulated by a subsequent decrease of the pressure to 14 kPa while keeping $Ca_{actn} = 1.0$. The deformed mesh at end-ejection was saved as the ES mesh. Note that in a real heart the active tension in the fiber direction will decrease before end-ejection when the ventricular pressure starts to drop but the blood still keeps flowing out of the ventricle during the reduced ejection phase due to the inertia of the blood. Our model did not incorporate fluid mechanics. The influence of the fluid on the wall motion was only represented by the pressure, which was exerted on the endocardial surface of the mesh. Keeping $Ca_{actn} = 1.0$ and decreasing the pressure during the reduced ejection phase provided an ad hoc solution to simulate the (small) deformations that occurred during this phase.

2.9 Varying the Material Parameters

Table I lists the default parameter of the pole-zero law (1) and the active law (3) that were used in the simulations. Due to convergence problems during the simulations caused by high stress-gradients close to the base and particularly the apex, the material was made stiffer in these areas. This was implemented by setting the material parameters significantly stiffer for the apical nodes and slightly stiffer for the ring of nodes closest to the apex and for the base nodes. The default parameters in Table I were used for all other nodes. A linear interpolation of the parameters was used to obtain the parameter values within the different elements.

The three parameters for each term in (1) control the stiffness for one particular material direction. There is a large degree of coupling between the parameters within each term [15], [16], i.e. an increase of both k_1 and b_1 , or a decrease of a_1 will all increase the stiffness of the fiber direction. We were more interested in the general influence of variations of the material stiffness in each direction than the influence of each individual parameter per se. Thus, to study the effect of stiffer fibers all three parameters of the first term of (1) were changed 20% in a stiffer direction, i.e. the stiffer fiber parameters were: $k_1=1.2 \times 2.22$, $a_1=0.8 \times 0.475$, and $b_1=1.2 \times 1.5$ while the rest of the parameters were kept the same as in Table I. For softer fibers the three parameters were changed to 20% softer values: $k_1=0.8 \times 2.22$, $a_1=1.2 \times 0.474$, and $b_1=0.8 \times 1.5$. The default stress-strain relationships together with the 20% softer and stiffer relationships can be seen in Fig. 3 for the three axial directions. Simulations were first carried out as described above for the default parameters in Table I. Then in turn, the parameters of one term at the time of

Type	Axial properties		Shear properties	
Coefficients	k_1	2.22 kPa	k_4	1.0 kPa
	k_2	2.22 kPa	k_5	1.0 kPa
	k_3	2.22 kPa	k_6	1.0 kPa
Poles	a_1	0.475	a_4	0.8
	a_2	0.619	a_5	0.8
	a_3	0.943	a_6	0.8
Curvatures	b_1	1.5	b_4	1.2
	b_2	1.5	b_5	1.2
	b_3	0.442	b_6	1.2

Active law:
 $T_{\text{ref}} = 100\text{kPa}$ $\beta = 1.45$ $[\text{Ca}^{2+}]_{\text{max}} = 1$ $h = 1$ $c_{50} = 0.5$

Table I. Default material parameters used for the passive pole-zero law and the steady state active law.

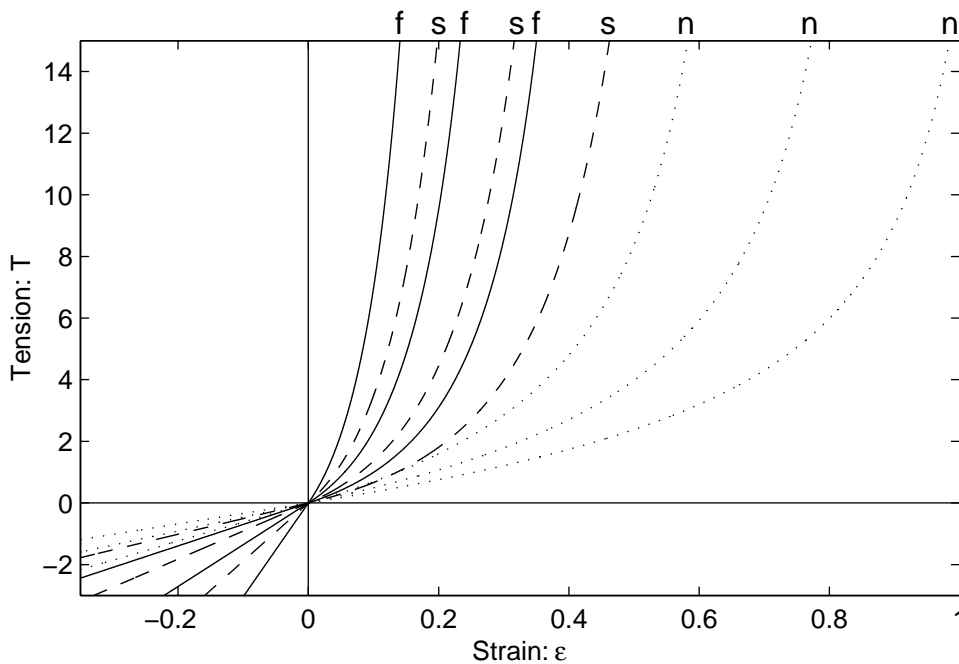


Figure 3. Stress-strain relationships in the fiber (f) direction - solid lines, sheet (s) direction - dashed lines, and sheet-normal (n) direction - dotted lines. The three lines in each direction are for the calculated relationships using three different sets of material parameters in the pole-zero law: default parameters (middle line), 20% softer parameters and 20% stiffer parameters.

(1) were changed and the simulation procedure repeated, both for 20% stiffer and 20% softer parameter values. For the 6 terms there were thus 12 different simulation results plus the result from using the default parameters. Note that also the material parameter

in the apical and basal regions were changed 20% in each case. Two additional simulations were performed: one with all material parameters changed to 20% stiffer values for all six terms of (1) and one with default parameters but where the myocardial wall was made approximately 20% thicker. The last test was performed to investigate the effect of a change of wall thickness on the deformation. The wall thickness was changed by moving the epicardial nodes out while the endocardial node positions were kept unchanged.

2.10 Mode Decomposition

For the mode decomposition the mesh structure was changed to be consistent with [3] where only one element was used in the transmural direction as opposed to three. This was done by removing the two sets of mid-wall nodes and stretching the elements from the endocardial to the epicardial nodes in the transmural direction. The ES mesh was translated along the x-axis (long-axis) so that the epicardial apex nodes of both the ES and ED mesh were at the same point. There was an order of magnitude or more difference between the field value, u , (where u is the x , y , or z coordinate) and its derivatives $\partial u/\partial \xi_1$, $\partial u/\partial \xi_2$, and $\partial^2 u/(\partial \xi_1 \partial \xi_2)$. This potential scaling problem was eliminated by subdividing the mesh in the circumferential and longitudinal directions, giving a mesh structure of 12 circumferential and 12 longitudinal elements and a total of 290 nodes. Discarding the nodal derivative information, only the nodal x , y , and z coordinates were used for the mode analysis.

In this study a symmetric truncated elliptical mesh was used which reduced the number of deformation modes compared with [3] where also asymmetric modes of deformation were included. The following deformation modes were selected: 1) longitudinal shortening, 2) wall-thickening, 3) “hinging” (where the apex serves as a hinge), 4) twisting of epicardial base, 5) twisting of endocardial apex, and 6) twisting of epicardial apex. An illustration of these modes is given in Fig. 4.

To extract the specific modes the nodal coordinates were first converted from rectangular Cartesian (RC) coordinates to prolate spheroidal (PS) coordinates, see (4), as the PS coordinate axes were aligned in the circumferential (θ), longitudinal (μ), and radial (λ) directions of the LV. The PS coordinates thus provided an easy mechanism for changing the nodes positions in one of the respective heart coordinate directions: Changing the μ -coordinates of the nodes changed the base-apex length of the mesh, changing the λ -coordinate changed wall-thickness/transmural position of the wall, and changing the θ -coordinate created a twisting/rotation mode of the mesh. The focus, f , of the PS coordinate system was calculated by looking at the node corresponding to the epicardial free-wall at equator where $\mu=90^\circ$ and $\theta=180^\circ$. λ was set to 1. The focus was then calculated by rearranging (4b). After the mode had been created by changing the mesh's PS coordinates, the new node coordinates were converted back to RC coordinates.

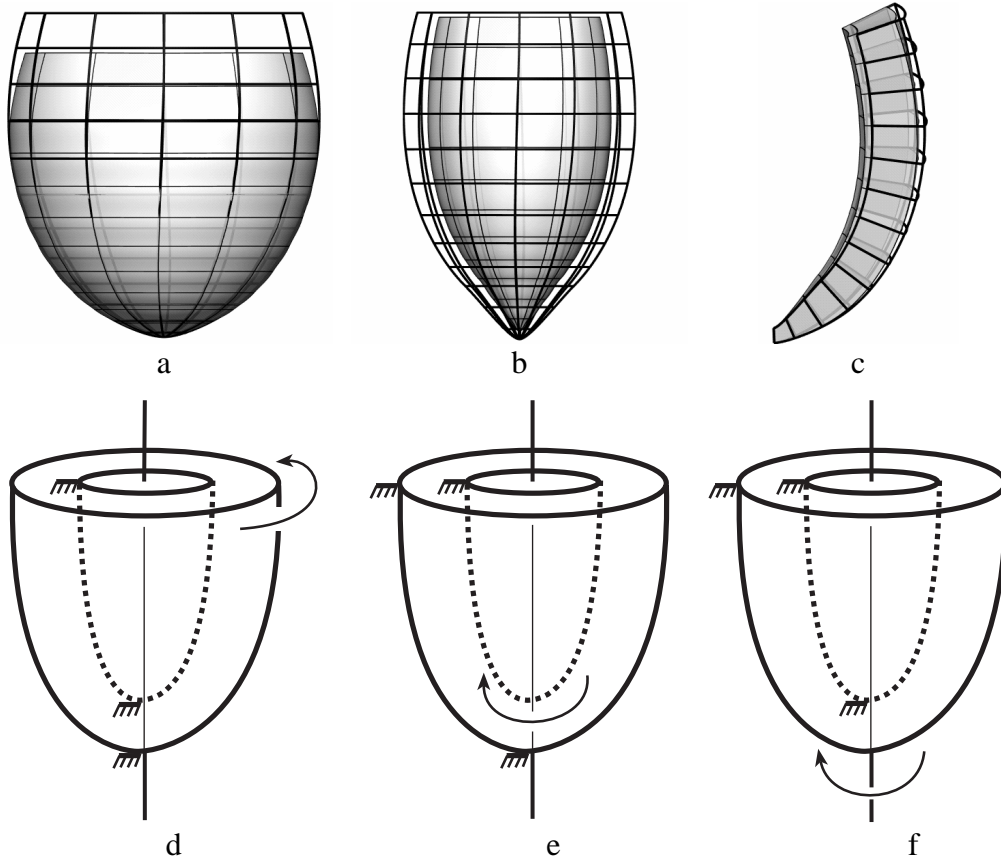


Figure 4. The 6 created deformation modes. In a)-c) the thick lines correspond to the original ED mesh while the thin lines and shaded surfaces correspond to the mesh created for the respective deformation mode. a) Longitudinal shortening mode, illustrated at the epicardial surface. b) Wall thickening mode, the endocardial surface is moved inwards (the epicardial surface, not shown, is left unchanged). c) Hinge mode, illustrated by a longitudinal slice of elements. d) Twisting of the epicardial base, illustrated by a schematic of the LV where the epicardial surface is rotated at the base with gradually decreasing rotation towards apex while the endocardial surface is fixed. e) Twisting of the endocardial apex. f) Twisting of the epicardial apex.

$$\begin{aligned}
 x &= f \cdot \cosh(\lambda) \cos(\mu) \\
 y &= f \cdot \sinh(\lambda) \sin(\mu) \cos(\theta) \\
 z &= f \cdot \sinh(\lambda) \sin(\mu) \sin(\theta)
 \end{aligned} \tag{4}$$

By using the ED mesh as starting mesh for extraction of each mode, the nodes of the ED mesh were changed accordingly. The longitudinal shortening mode was created by decreasing the μ -coordinate of the ED mesh base nodes by $\Delta\mu = -10.5^\circ$. The $\Delta\mu$ increment of the other nodes further down towards the apex were decreased linearly as a function of their row number, where rows were considered to be circumferential rings of nodes at the same longitudinal position. Row 1 was the row of nodes closest to the apex and row 12 was the base nodes (r_{base}). $\Delta\mu$ for the nodes on row r was then calculated as

follows: $\Delta\mu = -10.5^\circ * r/r_{\text{base}}$. A feature of the PS coordinates is that a change of the nodal μ -value whilst keeping λ and θ fixed will move the node along elliptical lines. This resulted in the base nodes not only moved downwards but also outwards as their μ -value was decreased and thus increasing the base area. This was the opposite of what was actually seen occurring at the base between ED and ES. This problem was solved by keeping the y and z values unchanged for the nodes with a μ -value over 90° (i.e. the nodes above equator) as they were before converting them to PS coordinates. The change of the μ -value for these nodes thus only changed the x-coordinate, which resulted in a movement straight up and down. The nodes below equator were moved along elliptical lines, which corresponded well with what we observed.

The second mode was wall thickening. The epicardial nodes were fixed while the endocardial nodes were changed by $\Delta\lambda = -0.1$. The third mode was a hinge mode where the cavity volume was increased by fixing the apex nodes and moving the higher nodes in by $\Delta\lambda = -0.05 * r/r_{\text{base}}$.

Mode 4 was the first twist mode where the endocardial nodes were fixed together with the epicardial apex node. The epicardial base nodes were rotated with the maximum angle of $\Delta\theta = -7^\circ$. The $\Delta\theta$ increment for the epicardial nodes closer to the apex varied linearly with their row number: $\Delta\theta = -7^\circ * r/r_{\text{base}}$. Mode 5 was a twist mode of the endocardial apex while all epicardial nodes were fixed. The boundary conditions for the simulations prevented any rotation of the endocardial base nodes. As a result the nodes immediately below the base rotated slightly clockwise when viewed from the apex while the nodes below the equator rotated counterclockwise with a higher rotation the closer they were to the apex. For mode 5 the endocardial nodes closest to the apex were rotated by $\Delta\theta = 15^\circ$ and this increment decreased linearly to 0 at the row of nodes at the equator ($r=9$) and to a negative $\Delta\theta = -2^\circ$ for the two rows just below the base ($r=10, 11$). For mode 6, the endocardial nodes were fixed while the epicardial nodes closest to the apex were rotated $\Delta\theta = 32^\circ$ and the increment varied linearly to 0 towards the base. The separation of the longitudinal twisting into these 3 modes incorporated both circumferential-longitudinal shearing as well as circumferential-radial shearing.

2.11 Calculating the Coefficients

The x, y, and z coordinates at each of the $N=290$ nodes of the subdivided ED mesh were entered in a column vector: $\mathbf{x}_{ED} = [x_1, y_1, z_1, \dots, z_N]^T$, where T is the transpose operator. A similar vector was constructed for the ES mesh: \mathbf{x}_{ES} . The coordinates of the created mesh for mode m were entered into vector \mathbf{x}_m . The total deformation could then be approximated by (5) where the mode coefficient, k_m , quantified mode m.

$$\mathbf{x}_{ES} - \mathbf{x}_{ED} \approx \sum_m k_m (\mathbf{x}_m - \mathbf{x}_{ED}) \quad (5)$$

A least-squares calculation was used to calculate the coefficients, k_m , as shown in (6) where M is the number of modes. Note that this approach linearizes the deviations about a set of mean deformations.

E-12

$$D = \begin{bmatrix} | & | & & | \\ \mathbf{x}_1 - \mathbf{x}_{ED} & \mathbf{x}_2 - \mathbf{x}_{ED} & \cdots & \mathbf{x}_M - \mathbf{x}_{ED} \\ | & | & & | \end{bmatrix}, \quad \mathbf{k} = \begin{bmatrix} k_1 \\ k_2 \\ \vdots \\ k_M \end{bmatrix} \quad (6)$$

$$\mathbf{k} = (D^T D)^{-1} D^T (\mathbf{x}_{ES} - \mathbf{x}_{ED})$$

2.12 Calculating Ejection Fraction

The cavity volume was extracted from the ED and ES mesh configurations as V_{ED} and V_{ES} , respectively. The ejection fraction (EF) was calculated as $EF = (V_{ED} - V_{ES})/V_{ED}$ for each simulation case.

2.13 Validation

The goodness of the approximation of (5) to the total deformation was checked by comparing the “true” ES mesh from the simulation with the approximated ES mesh obtained by rearranging (5) and using the calculated coefficients. The average Euclidean distance between the nodes of the two meshes, as shown in (7), was used as a measure for the goodness of the approximation. In (7) N is the number of nodes, x_{tn} is the x coordinate at node n for the “true” mesh while x_{mn} is the equivalent for the mesh obtained from (5).

$$E = \frac{1}{N} \sum_{n=1}^N \sqrt{(x_{mn} - x_{tn})^2 + (y_{mn} - y_{tn})^2 + (z_{mn} - z_{tn})^2} \quad (7)$$

3 Results

There was generally a consistent relationship between the calculated mode coefficient k_i obtained with default, softer, and stiffer parameters in the different material directions, i.e. when k_i was decreased for the stiffer parameters, k_i was increased for the softer parameters compared with the k_i obtained with default parameters. Table II shows the calculated coefficients for the different parameter sets. The hinge mode coefficient, k_3 , was small in all cases and this deformation mode was thus considered to be insignificant to the total deformation. The most significant change in the deformation modes for variation of the fiber stiffness was the wall thickening that was moderately reduced for increased stiffness. Variation of the sheet stiffness had a high impact on several modes with reduced longitudinal shortening, wall thickening, and epicardial base twist for stiffer properties. Stiffness variations in the sheet-normal direction showed little impact on the mode coefficients except a moderate decrease of longitudinal shortening for stiffer properties. Changing the parameters of the 1-2 shear (F-S) term of (1) had an impact of two of the twisting modes and moderate influence on the longitudinal shortening. Variations of the 1-3 shear parameters (F-N) had very small impact on the calculated coefficients. Variations of the 2-3 shear (S-N) stiffness had an impact on two of the twist modes and also showed more wall thickening for softer parameter values.

	k ₁	k ₂	k ₃	k ₄	k ₅	k ₆	EF
Default	1.00	1.00	0.11	1.00	1.00	1.00	51%
F stiffer	1.02	0.92	-0.09	0.95	0.92	0.94	48%
F softer	0.97	1.06	0.28	1.05	1.03	1.04	54%
S stiffer	0.85	0.77	-0.07	0.70	1.02	0.97	42%
S softer	1.17	1.20	0.14	1.43	0.91	1.00	58%
N stiffer	0.95	1.01	0.13	1.02	0.99	0.98	51%
N softer	1.04	0.99	0.08	0.99	1.00	1.01	51%
F-S stiffer	1.05	1.00	0.12	0.89	1.10	1.00	52%
F-S softer	0.97	1.00	0.09	1.05	0.95	1.00	51%
F-N stiffer	0.99	1.01	0.09	0.97	1.01	1.00	51%
F-N softer	1.00	1.00	0.13	1.04	0.98	0.99	51%
S-N stiffer	0.98	0.92	-0.14	1.28	0.97	0.94	47%
S-N softer	1.02	1.05	0.27	0.77	1.01	1.03	54%
All stiffer	0.84	0.69	-0.30	0.73	1.02	0.85	37%
Thick wall	0.86	1.15	-0.05	1.14	0.95	1.11	54%

Table II. Calculated mode coefficients for variations in the material parameter values along the different material directions: F=fiber, S=sheet, and N=sheet-normal. The coefficient values are normalized with respect to the coefficients obtained with default material parameters except for the k₃ values as the calculated k₃ values were so small that this mode was considered insignificant to the total deformation. The calculated coefficients for default parameters before normalization were: 0.93, 0.94, 0.11, 0.83, 0.96, and 1.00 for modes 1 to 6, respectively. Values that are $\pm 5\%$ or more different from the coefficient obtained with default material parameters are written with bold numbers. The last column shows the EF.

When all parameters were changed to stiffer values all the coefficients decreased except the endocardial-twisting coefficient, which was approximately unchanged. Using the default parameters with a thicker walled mesh resulted in different mode coefficients for all modes: The longitudinal shortening was decreased, the wall thickening was increased, the two epicardial twisting modes were increased whereas the endocardial twist was moderately decreased.

The EF was dramatically reduced from 51% with default parameters to 37% with stiffer material properties in all directions. It was also substantially reduced for stiffer sheets and moderately reduced for stiffer fibers and stiffer S-N shear parameters.

The Euclidean error between the nodes of the true ES meshes from the simulations and the approximated ES meshes obtained by rearranging (5) was 1.2 ± 0.6 mm (mean \pm SD). This was a relatively small error when considering that the LV mesh was of approximately the same size as that of an adult dog's LV.

4 Discussion

In this study we have used a previously developed method [3] to investigate LV deformation modes in an elliptical FE simulation model of the LV. Several simulations of the cardiac cycle from beginning of diastasis through to end of ejection were carried out with variations of the stiffness in the different material directions. The simulated deformation was decomposed and quantified into separate deformation modes for the different cases of material properties.

Variations of the fiber stiffness showed perhaps smaller influence on the deformation modes than one would expect. The generated active fiber stress may be dominating the passive properties during systole while the major influence on the deformation of the fiber stiffness compared to the other directions may occur during the passive inflation phase. During systole the active tension along the fibers will cause contraction of the fibers and expansion of the sheets that will result in wall thickening as the sheets are predominantly transmurally oriented. Increased fiber stiffness results in a steeper slope for compressive strains (Fig. 2) and reduces fiber contraction and thus wall thickening, which is consistent with the reduced k_2 for stiffer fibers. Higher sheet stiffness will resist expansion of the sheets and thus also decrease the wall thickening, which explains the reduced k_2 for stiffer sheets. A stretch in the sheet direction will cause a contraction in the sheet-normal direction due to incompressibility of the material, and as the sheet-normal direction is mainly aligned with the longitudinal direction particularly at the mid-wall, this will contribute to the longitudinal shortening. With higher sheet stiffness and less expansion of the sheets there will be less compression in the sheet-normal direction and as a result less longitudinal shortening will occur during fiber contraction. This mechanism may explain the reduction of k_1 for stiffer sheets. The stiffness in the sheet-normal direction is relatively much softer than in the fiber and sheet direction due to the low amount of connective tissue tying the sheets together. The deformation may thus be limited by the fiber and sheet stiffness and not as much the sheet-normal stiffness, which may explain the low influence of the sheet-normal parameters. Only a moderate change of the longitudinal shortening was affected by sheet-normal stiffness variations.

The results from variations of the shear strains are more difficult to interpret due to the complex orientation of the fiber-sheet orientations through the wall and the symmetry of the shear strains ($e_{ij} = e_{ji}$ for $j \neq i$). Due to this symmetry there are only 3 shear terms in (1). According to [6] the only shear term that are directly related to radial strain (i.e. wall thickening and k_2) is $e_{23} = e_{sn}$. This corresponded well with our results where stiffer S-N shear parameters resulted in a smaller k_2 . Increasing the F-S shear stiffness caused a moderate increase of the longitudinal shortening. An explanation for this may be that when the F-S shear stiffness is increased, F-S shearing is decreased and the deformation takes other forms that are more favorable energy-wise. Increased longitudinal shortening for the case of increased F-S shear parameters may be due to increased fiber shortening as the fibers, and thus the sheet, are predominantly longitudinally oriented at the subendocardium and extra shortening would contribute to longitudinal shortening. A change of deformation type like this may explain the few cases where a deformation

mode seemed to increase when the material properties in one direction were made stiffer (k_1 and k_5 for stiffer F-S shear properties and k_4 for stiffer S-N shear properties).

Young et al. [17] found that a group of patients with hypertrophic cardiomyopathy had decreased longitudinal shortening, approximately similar radial strains (wall thickening), and increased longitudinal torsion when compared with a group of normal subjects. Ho et al. [18] found an increased EF in a group of subjects with hypertrophic LV compared with a control group. Our thicker walled mesh showed similar behavior with reduction in longitudinal shortening, increase of the two epicardial twisting modes, and a moderately increased EF, but in contrast to [17] our results showed an increased wall thickening and a moderate reduction of endocardial twisting.

The EF was only related to the longitudinal shortening and wall-thickening modes in our model as the hinge mode was considered insignificant. The EF varied consistently together with these two modes for the various cases of stiffer material parameters.

Our model of the LV is highly simplified. Variation of the wall thickness showed an impact on the deformation and other geometric changes may also give different results. The fiber and sheet angles had the same transmural variation over the whole mesh while in reality there are substantial regional variations [7]. The impact of the pericardial sac, papillary muscles and right ventricle was not included in the model. Despite the approximations of the model used in this study the derived results seem reasonable in relation to the microstructural architecture and orientation and correspond well with other published results. We believe the simulation results provide at least qualitative data on the influence of the material properties on LV deformation.

Acknowledgement

The authors would like to thank Dr. Martyn Nash for his help with the FE program CMISS used in this study.

References

- [1] K. D. Costa, J. W. Holmes, A. D. McCulloch, "Modeling cardiac mechanical properties in three dimensions," *Phil. Trans. R. Soc. London A*, vol. 359, pp. 1233-50, Jun. 2001.
- [2] W. Colucci, D. Price, "Cardiac Tumors, Cardiac Manifestations of Systemic Diseases, and Traumatic Cardiac Injury", in *Harrison's Online*, Ed. K. Isselbacher, J. Wilson, J. Martin, McGraw-Hill, 2003, chap. 240, pp. 8. Available: <http://harrisons.accessmedicine.com/>
- [3] E. W. Remme, A. A. Young, K. F. Augenstein, P. J. Hunter, "Extraction and quantification of left ventricular deformation modes", *IEEE Trans. Biomed. Eng.*, Accepted, 2004.

- [4] I. J. LeGrice, P. J. Hunter, B. H. Smaill, "Laminar structure of the heart: a mathematical model," *Am. J. Physiol.*, vol. 272, pp. H2466-2476, May 1997.
- [5] I. J. LeGrice, Y. Takayama, J. W. Covell, "Transverse shear along myocardial cleavage planes provides a mechanism for normal systolic wall thickening," *Circ. Res.* vol. 77, pp. 182-93, Jul. 1995.
- [6] K. D. Costa, Y. Takayama, A. D. McCulloch, J. W. Covell, "Laminar fiber architecture and three-dimensional systolic mechanics in canine ventricular myocardium," *Am. J. Physiol.*, vol. 276, pp. H595-607, Feb. 1999.
- [7] M. P. Nash, P. J. Hunter, "Computational mechanics of the heart: from tissue structure to ventricular function," *J. Elasticity*, vol. 61, pp. 113-141, 2000.
- [8] P. M. Nielsen, I. J. LeGrice, B. H. Smaill, P. J. Hunter, "Mathematical model of geometry and fibrous structure of the heart," *Am. J. Physiol.*, vol. 260, pp. H1365-1378, Apr. 1991.
- [9] P. J. Hunter, "Myocardial constitutive laws for continuum mechanics models of the heart," *Adv. Exp. Med. Biol.*, vol. 382, pp. 303-318, 1995.
- [10] P. J. Hunter, M. P. Nash, G. B. Sands, "Computational electromechanics of the heart," in *Computational Biology of the Heart*, A.V. Panfilov and A.V. Holden, Ed., West Sussex, England: John Wiley & Sons Ltd, 1997, chap. 12, pp. 345-407.
- [11] J. H. Omens, Y. C. Fung, "Residual strain in the rat left ventricle," *Circ. Res.*, vol. 66, pp. 37-45, Jan. 1990.
- [12] E. K Rodriguez, A. Hoger, A. D. McCulloch, "Stress-dependent finite growth in soft elastic tissue," *J. Biomech.*, vol. 27, pp. 455-467, Apr. 1994.
- [13] K. D. Costa, K. May-Newman, D. Farr, W. G. O'Dell, A.D. McCulloch, J. H. Omens, "Three-dimensional residual strain in midanterior canine left ventricle," *Am. J. Physiol.*, vol. 273, pp. H1968-H1976, Oct. 1997.
- [14] A. M. Katz, *Physiology of the heart*, 2nd ed. New York: Raven Press, 1992. (a): pp. 362, (b): pp. 407.
- [15] C. Stevens, E. Remme, I. LeGrice, I., P. Hunter, "Ventricular mechanics in diastole: material parameter sensitivity," *J. Biomech.*, vol. 36, pp. 737-748, May 2003.
- [16] E. W. Remme, P. J. Hunter, O. Smiseth, C. Stevens, S. I. Rabben, H. Skulstad, B. Angelsen, "Development of an *in vivo* method for determining material properties of passive myocardium," *J. Biomech.*, vol. 37, pp. 669-678, May 2004.
- [17] A. A. Young, C. M. Kramer, V. A. Ferrari, L. Axel, Reichek N, "Three-dimensional left ventricular deformation in hypertrophic cardiomyopathy," *Circ.*, vol. 90, pp. 854-867, Aug. 1994.
- [18] C. Y. Ho, N. K. Sweitzer, B. McDonough, B. J. Maron, S. A. Casey, J. G. Seidman, C. E. Seidman, S. D. Solomon, "Assessment of diastolic function with Doppler tissue imaging to predict genotype in preclinical hypertrophic cardiomyopathy," *Circ.*, vol. 105, pp. 2992-2997, Jun. 2002.